Parameterized internal wave mixing in three ocean general circulation models

Nils Brüggemann[1], Martin Losch[2], Patrick Scholz[2], Friederike Pollmann[4], Sergey Danilov[2], Oliver Gutjahr[1], Johann Jungclaus[1], Nikolay Koldunov[2], Peter Korn[1], Dirk Olbers[2,3], Carsten Eden[4]

[1]Max Planck Institute for Meteorology, Hamburg, Germany
[2]AWI, Bremerhaven, Germany
[3]Universität Bremen, Germany
[4]Institut für Meereskunde, Universität Hamburg, Germany

Key Points:

- the IDEMIX parameterization for internal wave mixing is evaluated in three global ocean models using three different tidal forcing
- in agreement with observations, simulations using IDEMIX show stronger and spatially more variable mixing patterns than those without IDEMIX
- most circulation and water mass changes can be attributed to stronger mixing but some effects are likely blurred by numerical mixing

Corresponding author: Nils Brüggemann, `nils.brueggemann@mpimet.mpg.de`

Abstract

The parameterization IDEMIX for vertical mixing by breaking internal gravity waves is evaluated in three different non-eddy resolving ocean models. Three different products of wave forcing by tidal flow over topography, representing the current uncertainty, are applied and compared to reference simulations without IDEMIX, allowing the model-independent effects of the new closure to be assessed. Common to all models is larger interior mixing work with stronger horizontal structure due to the inhomogeneous forcing functions in all simulations using IDEMIX, in better agreement to observations. Coherent model responses to the stronger mixing work are changes in the thermocline depth including IDEMIX related to stronger shallow overturning cells in the Indo-Pacific Ocean. Furthermore, deeper mixed layer depths in the subpolar North Atlantic are related to an increase of the Atlantic overturning circulation which brings the model closer to observations, coming along with an increase in northward heat transport. In the Southern Ocean, excessive energy input by one of the forcing products leads to unrealistic deep convection in the Weddell Sea in one of the models. The deep Indo-Pacific overturning circulation and the bottom cell of the Atlantic feature an incoherent model response, which may point towards the importance of excessive numerical mixing in the models.

Plain Language Summary

Gravity waves propagate not only at the ocean's surface but also in the ocean interior. These internal gravity waves are generated mostly at the bottom by oscillating tidal flow across topographic obstacles. Similar to the surface waves, the internal waves can break and mix the surrounding water when the waves get shorter but their amplitude remains the same. Such interior wave breaking mixes dense water upwards which is important to drive large-scale flows such as the global overturning circulation of the world's ocean.

Current ocean models cannot resolve the small-scale wave breaking. Therefore, this important effect needs to be implemented by a parameterization. In this study, we use the new parameterization IDEMIX which is based on internal wave dynamics and energetics. This parameterizations is implemented in three different ocean models. A necessary input for the IDEMIX parameterization is the energy input into the wave field at the bottom of the ocean. In this study, we use three different products for this energy input to study the sensitivity of the simulated circulation with respect to this forcing differences. Common model responses are diagnosed and discussed, while some incoherent model responses regarding the overturning circulation pose new questions.

1 Introduction

In the ocean's meridional overturning circulation, turbulent mixing is responsible for the return of abyssal dense water to the surface through the isopycnals, even though there is little turbulent energy available to drive substantial diapycnal flows (Munk & Wunsch, 1998). A lot of this mixing is thought to be associated with breaking internal waves. Internal waves are generated by, for instance, tidal or geostrophic flows over topography or by fluctuating winds (Olbers, 1983; Polzin & Lvov, 2011). While they propagate through the ocean they can become subject to non-linear wave-wave interactions through which energy is transferred to waves with smaller and smaller wave lengths until the waves become unstable, break and produce small-scale turbulence (see e.g. Müller et al., 1986). Unfortunately, the life cycle of an internal wave involves a large range of space and time scales, so that its observation or simulation poses many challenges (Müller et al., 1986). As a result, large uncertainties remain regarding the understanding and quantification of single aspects of this life cycle. Furthermore, many aspects of internal wave dynamics are not resolved in global ocean models used in state-of-the-art climate models and will most likely not be resolved in the foreseeable future. Instead, the effect of the internal wave breaking and the associated diapycnal mixing needs to be parameterized in these ocean models to account for the important driving mechanism of diapycnal flows.

Owing to the complexity of the problem and the sparsity of adequate observations, interior internal wave driven mixing is often treated rather simply in many ocean modelling endeavours. In particular, vertical mixing parameters are often chosen without taking into account physical or energetic constraints with respect to the sources of mixing. They are rather treated as tuning coefficients to optimize certain aspects of the respective model simulations. For some vertical mixing schemes like the PP (Pacanowski & Philander, 1981) or KPP (Large et al., 1994) scheme it is common practise to let the vertical diffusivity fall back in the interior to often spatially constant background values of $O(10^{-5}\,\mathrm{m}^2/\mathrm{s})$. An analogous approach in higher order mixing closures like the TKE scheme of Gaspar et al. (1990) is to impose an unphysically motivated minimal (constant) turbulent energy. The basic assumption behind both choices is that the internal wave field supplies a certain but unknown amount of energy to turbulent mixing, generating either the turbulent energy or the mixing rate itself. However, it is obvious that both approaches are not physically consistent with the dynamics of internal waves, and will not consistently represent the observed spatio-temporal variability of wave-induced turbulent mixing. Motivated by observations of enhanced mixing rates close to rough topography, Simmons et al. (2004) attempt to include this variability by using an ad-hoc length scale for the vertical shape and a map of tidal energy forcing for the horizontal distribution, to construct a three-dimensional field of mixing rates. However, this closure remains heuristic without considering wave physics, and the wave energy cycle is not treated consistently.

The Internal wave Dissipation, Energy and Mixing (IDEMIX) model (Olbers & Eden, 2013) is a parameterization framework built to consistently account for the internal wave physics. IDEMIX includes processes such as an energy flux into the internal wave field by tides, surface winds, and other forcing functions, horizontal and vertical propagation and refraction of internal waves, wave-wave interaction, wave-mean flow interaction, and the conversion of internal wave energy to small-scale turbulence associated with wave-breaking. The IDEMIX model, however, depends crucially on the forcing of tides and waves, but the magnitude and spatial pattern of these forcing functions bear large uncertainties. One aim of this study is thus to estimate the uncertainty of key aspects of the ocean circulation rooted in the uncertainty of the tidal forcing. To this end, we compare three simulations with different tidal forcing products applied to IDEMIX with reference simulations without IDEMIX, in which small-scale turbulence is parameterized by a constant minimum background value. The different forcing products are derived from (1) a scaling law for internal tide generation applied in barotropic ocean models using a bulk wave number for topography (Jayne & St. Laurent, 2001), (2) a direct calculation from linear theory applying a more realistic bottom topography and using eight tidal constituents from a tidal model (Nycander, 2005; Falahat et al., 2014) and (3) estimates of internal tide generation from a high-resolution ocean model (Li & von Storch, 2020) complemented with higher constituents from linear theory. The results are evaluated with respect to water mass biases, circulation changes, and mixing rates obtained from observations.

The effect of different parameterizations is often model dependent. To assess this effect, we apply three different representative state-of-the-art ocean models: ICON-O (Korn et al., 2022), FESOM (Danilov et al., 2017), and MITgcm (Marshall et al., 1997). The models are very similar in their implementation of IDEMIX, share the same surface forcing, and are similar albeit not equal in their vertical and horizontal resolution. The models also have substantial differences: most importantly, ICON and FESOM use (different) triangular grids in the horizontal, while the MITgcm uses a classical rectangular grid.

Table 1. Most important features of the numerical models used in this study. Note that the effective horizontal resolution is difficult to compare on the different grids. Here we simply give the nominal grid spacing.

	ICON-O	FESOM	MITgcm
horizontal resolution	ca. 40 km	ca. 20–100 km	ca. 20–111 km
vertical levels	64	48	50
grid type	triangular	triangular	rectangular
grid staggering	C-grid	B-grid	C-grid

ICON and the MITgcm use a C-grid discretization, while FESOM uses a B-grid. A complete description of similarities and differences of the three models is beyond the scope here, the reader is referred to the key references of the models given here and below. In any case, we aim to differentiate between model-independent effects of the IDEMIX closure with different forcings functions and the model-dependent effects by including three different models.

In the following section 2, we detail the model setups and parameter choices. In Section 3, we discuss the effect of the different internal wave forcing products in the different models on the mixing work and compare to available observations of mixing in Section 4. In Section 5 the simulated water masses and in Section 6 the impact on the circulation are discussed. Section 7 provides discussion and conclusion.

2 Numerical model configurations and experiments

We use in this study three different numerical models with similar configurations. These models are the MITgcm, FESOM and ICON-O. All configurations have been developed for other studies which do not include IDEMIX, and all model parameters are chosen according to their respective default values obtained from the previous general model performance tuning. Here we only unify the vertical mixing parameterizations in all models without retuning the models. Some important model features are listed in Tab. 1. In all models, meso-scale eddies are not resolved but parameterized by a bolus velocity (Gent et al., 1995) and isopycnal diffusion (Redi, 1982). ICON uses a constant thickness mixing coefficient, FESOM a vertically varying coefficient following Ferreira et al. (2005), and the MITgcm simulation uses a horizontally varying coefficient based on horizontal and vertical buoyancy gradients (Visbeck et al., 1997). Furthermore, all three models differ in the numerical implementation of the parameterization (Korn, 2018). The MITgcm and FESOM simulations use a vertical z^*-coordinate (Adcroft & Campin, 2004) while ICON uses z-levels. All models use a non-linear free surface. More details about the specific model configurations can be found for MITgcm, FESOM and ICON-O in Forget et al. (2015), Scholz et al. (2022), Korn et al. (2022), respectively.

All simulations are forced by the same wind stress, and surface heat and freshwater fluxes are computed with the same bulk formulae (Large & Yeager, 2009) from atmospheric fields of the 1958–2019 Japanese Re-Analysis dataset JRA55-do-v1.4.0 (Tsujino et al., 2018). For all simulations, the models are integrated for five consecutive forcing cycles of 62 years. In addition to applying freshwater fluxes, surface salinity is relaxed towards its initial condition with a piston velocity of $10\,\mathrm{m}/60\,\mathrm{days} = 0.1666\,\mathrm{m\,d^{-1}} = 1.929{\times}10^{-6}\,\mathrm{m\,s^{-1}}$. Initial conditions for temperature and salinity are also identical and derived from January values of the PHC-3.0 climatology (Steele et al., 2001). If not stated otherwise, we diagnose time averages over the last 40 years (1979–2019) of the last forcing cycle. While the total integration time of 310 years might be too short for the simulations to reach an equilibrium, it is still sufficiently long to study the major implications of vertical mixing on water masses and circulation.

For each model, we discuss four different experiments with different sources of internal wave energy available for mixing. In our reference configuration vertical mixing is parameterized by the higher order turbulent kinetic energy (TKE) closure by Gaspar et al. (1990) and Blanke and Delecluse (1993), without making use of IDEMIX (experiments FESOM-REF, ICON-REF, and MITgcm-REF, respectively). Here, the diapycnal interior mixing is determined by resetting the turbulent kinetic energy to a minimum background level. This approach implicitly assumes that an unknown internal wave field always provides this level of energy for mixing in the ocean interior. A detailed description of the closure by Gaspar et al. (1990) is given in Appendix A. In the other three experiments carried out with each model, we include the IDEMIX closure (Olbers & Eden, 2013), which predicts the propagation and dissipation of the wave energy, and the minimum background level of turbulent kinetic energy of the original TKE-scheme is accordingly set to zero. A detailed description of the IDEMIX closure is given in Appendix B.

Our version of IDEMIX requires surface and bottom wave forcing, given by the near-inertial wind-driven surface pumping and by interaction of barotropic tides with topography, respectively. In the sensitivity experiments with IDEMIX, the surface forcing remains the same, but we apply three different forcing datasets for the bottom forcing to reflect the current uncertainty of internal wave generation by the tides: the forcing as described in Jayne and St. Laurent (2001) (FESOM-A, ICON-A, MITgcm-A), the forcing derived from linear theory after Nycander (2005) (FESOM-B, ICON-B, and MITgcm-B), and the forcing derived to large parts from the STORMTIDE2 simulation (Li & von Storch, 2020) (FESOM-C, ICON-C, and MITgcm-C)

In the following, we only list the most important features of these three bottom forcing datasets and refer to a more detailed description in Appendix C. Forcing A (Fig. 1b) is based on a scaling law for internal tide generation (and barotropic tide dissipation) suggested by Jayne and St. Laurent (2001) that is motivated by linear theory (Bell, 1975b) and used in barotropic tidal models to represent the drag exerted by the baroclinic on the barotropic tide. The energy flux by this drag diagnosed from barotropic tidal models is often used in the heuristic parameterization of Simmons et al. (2004), for example, in the CESM model (Hurrell et al., 2013). One parameter in the scaling law is the bulk wavenumber of the bottom topography, which is treated as a tuning parameter in the barotropic tidal models. This means that the effect of bottom topography on the generation of internal tides may not be represented very accurately in forcing A, that is, forcing A is subject to (unknown) errors of the barotropic model.

To avoid this source of errors, one can alternatively derive the bottom forcing directly from linear theory and realistic bottom topography at high resolution. Here we use the estimates of Nycander (2005) as calculated by Falahat et al. (2014) (forcing B hereafter, Fig. 1c), which takes as input the barotropic velocities from a tidal model using the eight major tidal constituents and the observed topographic spectrum. Both forcings A and B are, however, subject to the limitations of linear theory. For example, linear theory breaks down for topographic slopes steeper than the internal tide beam.

Estimating the tidal bottom forcing from internal tide generation in ocean general circulation models that are forced by the full tidal potential avoids issues of linear theory entirely. As an example for this method, we derive forcing dataset C (Fig. 1d) from a concurrent simulation of circulation and tides by the Max Planck Institute Ocean Model referred to as STORMTIDE2 (see Li & von Storch, 2020, for details of the model setup and the computation of the internal tide generation). Restrictions of linear theory do not apply in such simulations, but the finite horizontal resolution (about 0.1^o) allows only the first few vertical internal wave modes to be excited, and the parameterization of dissipation may introduce additional unknown model errors. In addition, the conversion of-

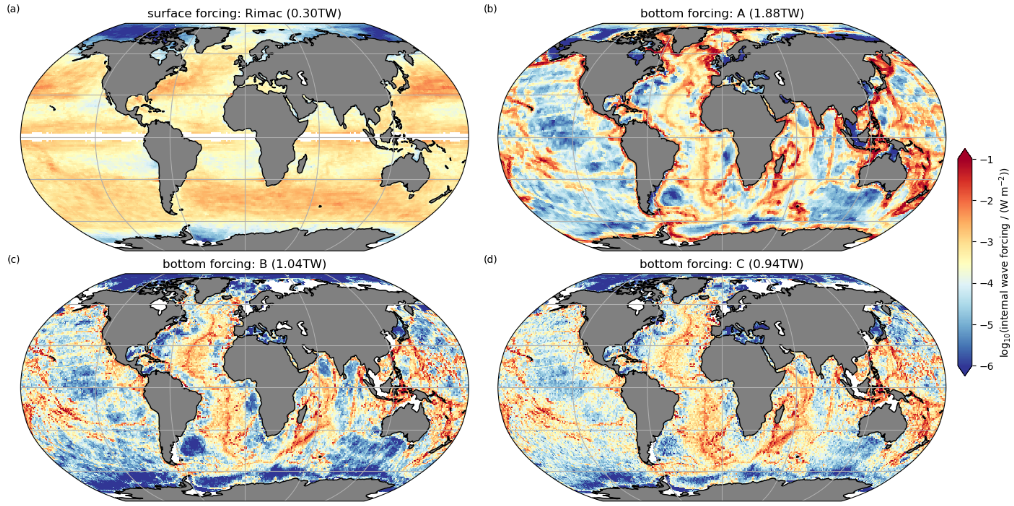

Figure 1. Energy flux into the internal wave field mapped to the ICON grid from (a) wind-driven near-inertial surface pumping (Rimac et al., 2013) and the bottom (tidal) forcings A-C (b-d). See text for more details.

ten becomes negative, which is not necessarily unphysical (Kelly & Nash, 2010) but means it cannot be used directly as a (per definition positive) forcing term in IDEMIX. We here follow the procedure of de Lavergne et al. (2019) to remove negative values while preserving the original depth-dependent conversion rate. The model simulation by Li and von Storch (2020) includes the full luni-solar tidal forcing. However, only the internal tide generation by the M_2 tide was calculated, so that the other seven constituents of the computation by Nycander (2005) are added to complete the forcing C. The model simulation includes full luni-solar tidal forcing. However only the internal tide generation by M2 tide was calculated. These seven constituents account for roughly a third of of the globally integrated conversion in forcing C. In summary, all three bottom forcing datasets have their own limitations and it is unclear a-priori which has the lowest biases and what the implications are on simulated circulation and watermass structure if the forcing is applied in a numerical model.

All tidal forcing datasets have in common that the energy flux is enhanced over major topographic obstacles like sea mounts and ridges, for example, along the Mid-Atlantic Ridge. The forcings B and C are in general smaller in magnitude than forcing A, especially in the Southern Ocean, and the global integral of forcing A (1.9 TW) is about two times larger than for B (1.0 TW) and C (0.9 TW). Note that the estimate of forcing B excludes supercritical slopes where linear theory breaks down and thus excludes depths above 400 m. In contrast, the forcing A includes also the continental shelves (Fig. 1b). In the model-based forcing C, there are no large conversion rates at the shelf break. This may point towards a bias of the barotropic models used to generate forcing A. A discussion of the reasons for the differences of the forcing datasets is beyond the scope of the current study; here we consider the differences as plausible error bounds for the bottom forcing.

Oscillations in the horizontal divergence of wind driven currents in the surface mixed layer with frequencies at or larger than the local Coriolis frequency generate downward propagating internal waves at the base of the mixed layer. This process is called (near-inertial) wind-driven surface (Ekman) pumping (Olbers et al., 2020; von Storch & Lüschow, 2023). For all simulations, we use the same associated energy flux into the internal wave

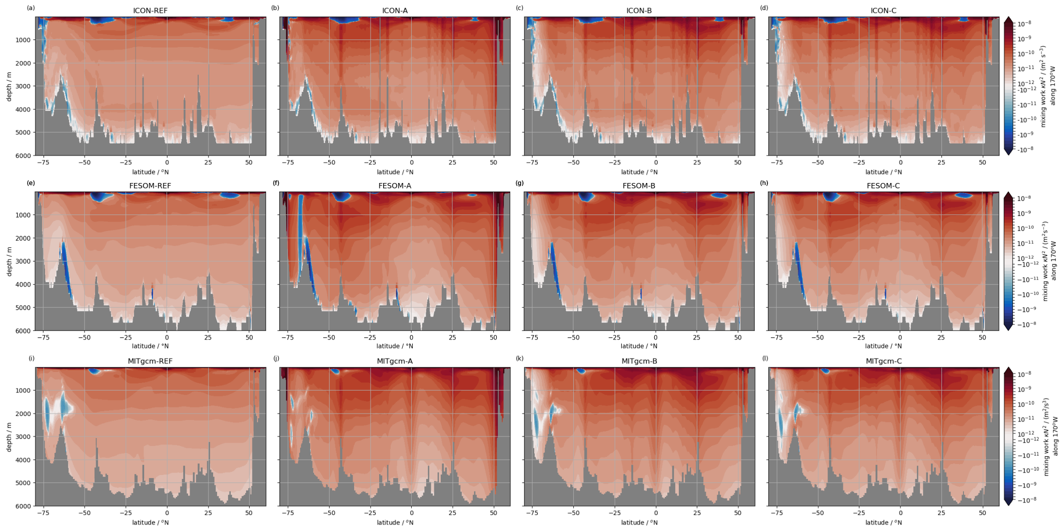

Figure 2. Mixing work κN^2 along a meridional section at 170^{o}W. First row (a-d) shows results from ICON, second row (e-h) those from FESOM and third row (i-l) those from the MIT-gcm.

field derived from the global estimate of Rimac et al. (2013) (Fig. 1a) since the global integral (0.3 TW) is much smaller than the tidal forcing (Fig. 1b–d).

3 Simulated mixing work

The main source of small-scale turbulence in the interior ocean is due internal wave breaking. Thus, the internal wave forcing controls the interior turbulent kinetic energy that is available for mixing of water mass properties. Note that in our reference experiments the internal wave breaking is parameterized by resetting small turbulent kinetic energy values to an arbitrary constant minimum, but in the simulations with IDEMIX, this source of energy is parameterized based on physical principles. There are two major sinks of turbulent energy in the interior ocean: molecular dissipation with subsequent transformation into heat, and upward mixing of dense water masses, which represents the transformation of turbulent kinetic to mean potential energy. The upward energy flux is given by κN^2, with the diapycnal diffusivity κ and the square of the buoyancy frequency N. In the following, we will refer to κN^2 as mixing work.

Fig. 2 shows the mixing work κN^2 along 170°W in the different experiments. In the surface mixed layer, κN^2 is low or even negative, but in the interior κN^2 is mostly positive. In the Southern Ocean close to the bottom, κN^2 is negative in all ICON and FESOM simulations (N^2 gets small or negative there, not shown). In FESOM-A, a large region with $\kappa N^2 < 0$ in the Southern Ocean extends even towards the surface. This is related to a potentially too strong wave forcing which effects also the mixed layer depth and circulation, and which will be further discussed below. In the MITgcm simulations, there are small and negative values of κN^2 at mid depth in the Southern Ocean (Fig. 2i–l) associated with the circulation in the Ross Sea. These features can be traced back to a feedback between vertical mixing and stratification in regions of strong horizontal flow: generally salinity stabilizes the water column and temperature destabilises it in this regions. When horizontal advection and vertical mixing reduces the small vertical salinity gradients they can no longer stabilize the water column leading to further mixing.

In general, the magnitude of the mixing work in the ocean interior is similar in all experiments: κN^2 decreases from $10^{-8}\,\mathrm{m^2/s^3}$ close to the surface to $10^{-11}\,\mathrm{m^2/s^3}$ at depth. In all experiments with IDEMIX, however, κN^2 tends to be larger compared to the respective reference experiment, in particular towards the surface. In all reference experiments, the parameterized homogeneous source of turbulence in the experiments ICON-REF, FESOM-REF, and MITgcm-REF yields a relatively homogeneous mixing, whose structure is mainly shaped by N^2. In contrast, the simulations including IDEMIX with different tidal forcings show a much richer horizontal structure with larger mixing work due to enhanced wave forcing over rough bathymetry. Differences for the individual models between the experiments with different tidal forcings are smaller than the difference to the respective reference experiment. The experiments with forcing A tend to have slightly larger κN^2 than those using the other forcings in accordance with the larger energy inputs, but all agree roughly in the location and magnitude of the mixing hot spots.

For the simulations including IDEMIX, the total energy available for mixing is the globally integrated internal wave forcing from Fig. 1, which amounts to 2.13, 1.27, and 1.18 TW for forcing A, B, and C, respectively (taking bottom and surface forcing together). For the reference simulations without IDEMIX, this available mixing energy is parameterized as the change of energy (per time) that is necessary to keep the turbulent kinetic energy at its depicted background value which in our case is $1 \times 10^{-6}\,\mathrm{m^2\,s^{-2}}$. Integrating this rate of change leads to a mixing work of 0.37, 0.28, and 0.25 TW for ICON-REF, FESOM-REF, and MITgcm-REF, respectively. We interpret these values as an energy supply to the interior turbulent kinetic energy, which can be compared with the total wave forcing in the simulations including IDEMIX. The mixing work in the reference simulations is thus by far lower than in the simulations including IDEMIX and of a similar magnitude as the wind induced forcing. In principle, we could increase the mixing work in the reference simulations by choosing a different background value for turbulent kinetic energy, but by doing so the observed horizontal structure with its mixing hot spots will not be reproduced in the reference simulation. Therefore, we keep the commonly used background parameter and make no attempt to change it.

The diapycnal diffusivities κ are shown in Fig. C1. Horizontal variations of κ are stronger when IDEMIX is applied comparable to the mixing work (Fig. 2). One exception is ICON-REF, where also an enhanced horizontal structure can be found, this structure is accompanied by a similar structure in N^2 (not shown) such that the product κN^2 is smooth (Fig. 2a). In all simulations, κ is enhanced in the upper ocean mixed layer. In ICON and FESOM, enhanced diffusivities can also be found at the bottom and in the Southern Ocean (in particular in FESOM-A, where the 170°W section cuts through the deep convection area in the Weddell Sea of this simulation). In the MITgcm simulations, the diffusivities are also enhanced in the Southern Ocean between 1000 m and 3000 m in accordance to the unstable conditions which occur in the simulations of this model (as discussed above). In general, all simulations with IDEMIX have higher diffusivities in accordance with the higher amount of energy available for mixing.

4 Comparing mixing work with observation

Direct observations of small-scale turbulent mixing are sparse. Therefore, we compare our model simulations to indirect estimates that were obtained from hydrographic profiles by applying the finestructure method (e.g. Gregg, 1989; Kunze et al., 2006; Polzin et al., 2014). The finestructure method links small-scale turbulence to finescale internal gravity wave variability based on a parameterization of wave energy dissipation by wave-wave interactions. Note that this parameterization is also used in IDEMIX and given by ϵ_{iw} in Eq. B1. This form for ϵ_{iw} is confirmed by numerical evaluation of the scattering integral for wave-wave interactions (Eden et al., 2019). The finestructure estimates have a substantially larger uncertainty (a factor of three and more) than microstructure or direct turbulence observations (Pollmann et al., 2017). We can therefore reliably com-

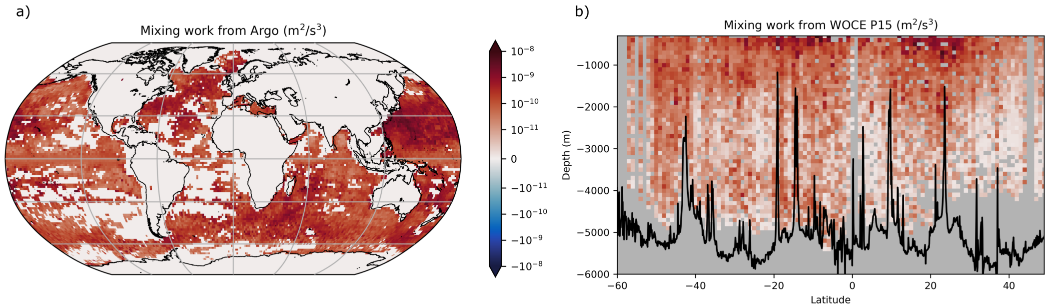

Figure 3. Mixing work κN^2 compiled from the finestructure estimates of (a) Pollmann et al. (2017) and (b) Kunze (2017). The data in (a) represent an average between 300 m and 2000 m depth. The data in (b) are averaged between 164.9^{o}W and 165.1^{o}W north of the equator and between 169.9^{o}W and 170.1^{o}W at and south of it (WOCE section P15). The black lines represent the topography from Becker et al. (2009) (SRTM30+), showing the 0 m-isobath in (a) and the bottom topography in (b).

pare the observed quantities to our model simulations only where variations in magnitudes are sufficiently large, that is, larger than the error bound of a factor of three. We here use (a) an estimate of the vertical diffusivity and TKE dissipation rates from Argo float profiles (Pollmann et al., 2017) and (b) a data base derived from the finestructure method applied to WOCE/CLIVAR hydrographic sections (Kunze, 2017) (Fig. 3).

The mixing work κN^2 varies geographically in the global ocean in the depth range accessible by Argo float observations (above 2000 m, Fig. 3a). The variations span several orders of magnitude, with relatively low values along the equator and over the abyssal plains and maxima near mixing hot spots associated with rough bottom topography (e.g. the Hawaiian and Emperor Seamount Chains and the Izu-Bonin-Mariana arc system) and eddy activity (e.g. the Gulf Stream and Kuroshio regions). The WOCE section P15 runs roughly along 170±5°W, so that we can compare the P15 κN^2 estimate (Kunze, 2017) (Fig. 3b), with Fig. 2 (note the different x-axis limits owing to limited data availability). By definition, the finestructure method is only applied where $N^2 > 0$, so in contrast to the model simulations, the mixing work contrary is always positive. The mixing work decreases with depth from maximum values of $10^{-8}\,\mathrm{m^2s^{-2}}$ near the surface to minimum values of $10^{-11}\,\mathrm{m^2s^{-2}}$ and less at intermediate depth and, in some locations, near the sea floor. This vertical structure and the overall magnitude is similar in all model simulations using IDEMIX.

In the horizontal, the observed mixing work shows four bands of elevated mixing work (κN^2) almost for the entire water column. These are located south of 40°, around 30°S, around 20°N, and roughly between 20°S and the equator. These variations are significant within the uncertainty of the finestructure method (Pollmann et al., 2017): When averaging the mixing work in the water column below 1000 m (that is, below the observed surface maxima and, in case of the model simulations, also minima) and in 5° latitude bands, it is elevated by a factor of 6.5 (40°-45°S), 5.2 (25°-30°S) and 7.3 (20°-25°N) relative to the equatorial band at 0°-5°N. For any of the 5° latitude bands between the equator and 20°S, the corresponding factor is between 3 and 4. At these locations, topographic features stand out from the otherwise small-scale roughness or almost plain surface of the sea floor: Near 40°S, the WOCE P15-section crosses Chatham Rise of Zealandia, near 25°S Louisville Ridge, near 20°N the Hawaiian Island Chain and the surrounding seamounts, and between the equator and roughly 20°S, there are the seamounts and islands of the Samoan Basin (e.g. Harris et al., 2014; Mortimer et al., 2017). These topographic fea-

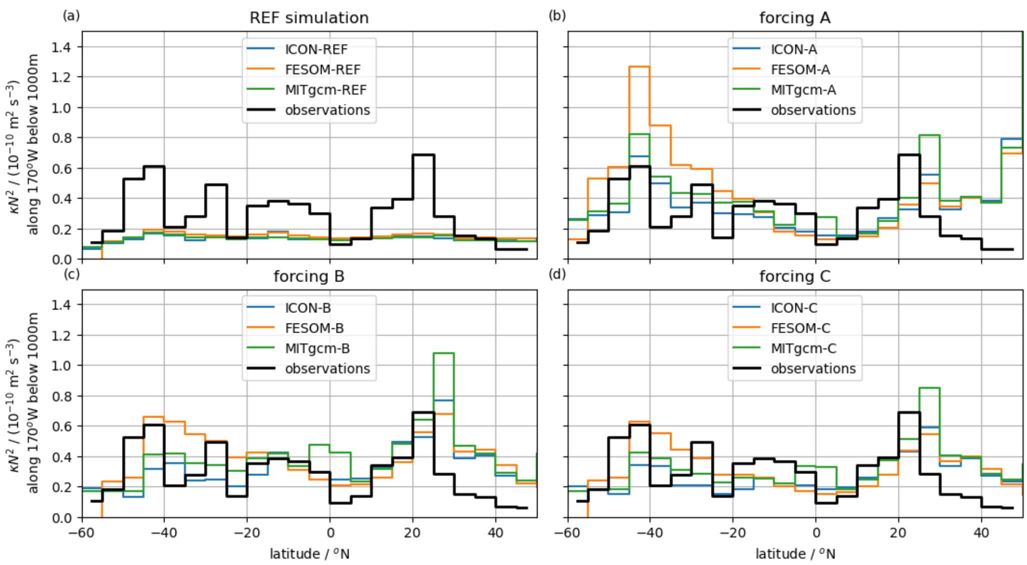

Figure 4. Mixing work along 170^{o}W averaged below 1000 m for the reference simulation (a) and the IDEMIX simulations with forcing data A, B, and C in (b), (c), (d), respectively. The black line represents the corresponding results for the observed mixing work shown in Fig. 3b. All results are binned in 5^o latitude intervals.

tures generate internal tides (Falahat et al., 2014, their Fig. 6), and, as some fraction of the generated baroclinic tidal energy is dissipated locally (Vic et al., 2019, their Fig. 5), hence the observed increase of mixing work κN^2.

These characteristics are reproduced in ICON, FESOM, and MITgcm to a different degree depending on the model and the forcing, but they are only reproduced when IDEMIX is active (Fig. 4): Without IDEMIX, the variability of the modeled κN^2 along 170°W is almost negligible compared to the observed one (Fig. Fig. 4a) and the modeled values are also notably lower. With IDEMIX, however, all models show a higher mixing work and reproduce the minima at higher latitudes and near the equator as well as the maxima at around 45°S and 20°N (Fig. 4b–d).

The increase in mixing work in high-mixing bands compared to the 0-5°N band is up to a factor of 2 (MITgcm), a factor of 2-3 (ICON) and a factor of 2-3 (FESOM, reaching a factor of 7 for forcing A) with IDEMIX, and below 30 % in the reference case without IDEMIX. The other two maxima of κN^2 seen in the observations are not reproduced by the models, with exception of the ICON simulation, which features a third peak just south of the equator for forcing B and forcing C. There might be several explanations for this, one being that the forcing itself is not as strong as at the other two locations where elevated mixing work is observed along 170°W (see Fig. 1).

Although the agreement between modeled and observed variability differs between the different forcing setups, a robust conclusion as to which forcing data leads to the best agreement with observations cannot be drawn owing to the relatively large uncertainty of the finestructure method. Moreover, there is also some spread among the models, and elevated mixing work south of the equator in FESOM for forcing A.

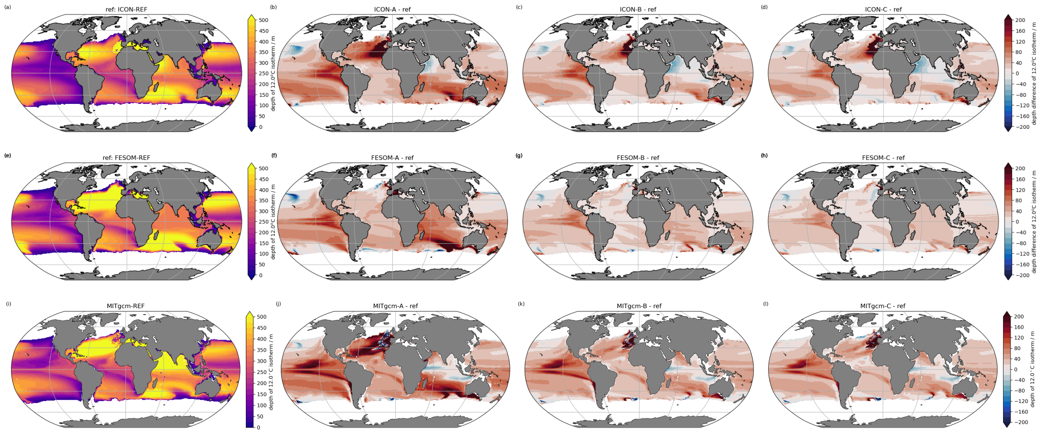

Figure 5. Depth of the 12^oC isotherm as an indication of the thermocline depth. First row (a-d) shows results from ICON-O, second row (e-h) FESOM, and third row (i-l) MITgcm. The first column shows results for the respective reference simulation, the other three columns show differences to the respective reference simulation.

5 Effects on water masses

The different levels of energy available for mixing have implications for water mass transformations in the model simulations. We choose the depth of the 12^oC isotherm as a proxy for the thermocline depth. More mixing work moves the thermocline downwards and less mixing lifts this isotherm upwards. With more mixing work available, all simulations that include IDEMIX have generally deeper thermoclines compared to the reference simulations (Fig. 5). The differences are not uniform and there are even locally shallower thermoclines with IDEMIX. For all three models, the deepest thermoclines can be found in the simulations with the strongest forcing A. Simulations with forcing B or C have comparable thermocline depths, in between those of the reference simulations and the simulations with forcing A. All models and all tidal forcings produce comparable differences of the thermocline depth when compared with the reference simulations. The strongest increase of the thermocline depth can be found in the eastern tropical Pacific, the eastern sub-tropical Atlantic and the southern Indian Ocean, but those areas are not necessarily related to enhanced tidal forcing and wave dissipation. The small regions of shallower thermocline depths also coincide between the different model simulations, showing a rather coherent model response in the thermocline to the change in vertical mixing.

Fig. 6 shows zonally averaged temperature biases compared to the initial conditions in the different simulations. While ICON-REF is too cold within the thermocline and too warm close to the surface within 50°S and 50°N, the other models are too warm within the thermocline and too cold at the surface in the reference simulations. The stronger mixing in the IDEMIX simulations changes these biases, since stronger upper-ocean mixing decreases surface temperatures and increase temperatures within the thermocline. For the ICON model, where thermocline waters are too cold in the reference simulation, the biases are reduced when IDEMIX is included (improvement is largest for ICON-A and less for ICON-B and ICON-C). For the other two models (FESOM and MITgcm), for which the thermocline waters are already too warm in the reference simulations, including IDEMIX increases these biases even further.

A prominent temperature bias which does not change with IDEMIX is located in the North Atlantic at 50°N (Fig. C2). All models with all forcing products are too warm

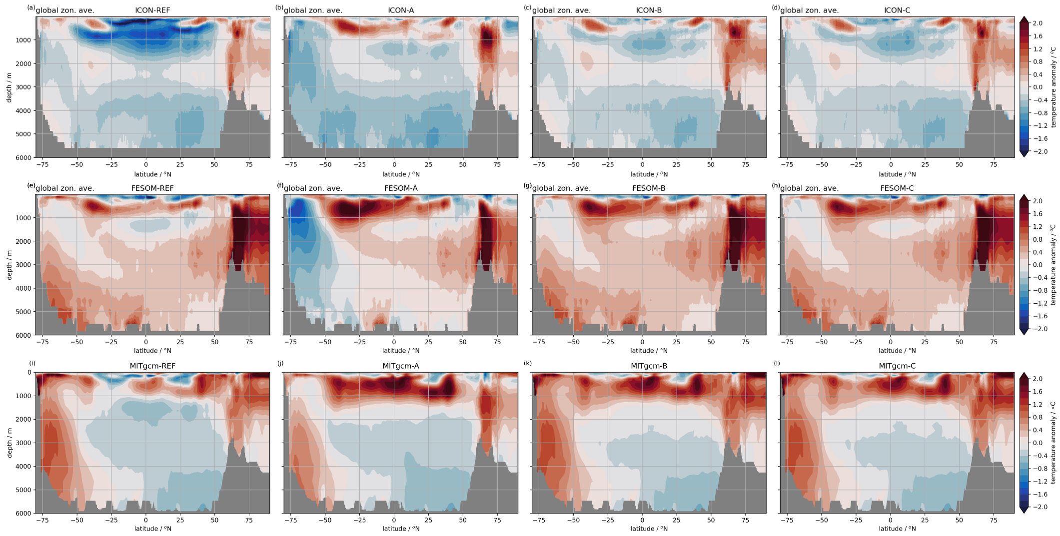

Figure 6. Zonal average of the temperature bias with respect to the observed initial conditions for ICON (a-d), FESOM (e-h) and MITgcm (i-l).

in this area and it appears that there are no fundamental changes when IDEMIX is applied. This bias is related to the (missing) north-west corner of the North Atlantic Current, whose dynamics is most likely related to (the interaction of) meso-scale eddies, topography, and dense bottow flow. The horizontal model resolutions do not allow to resolve mesoscale eddies, and the eddy closure used in the models is not designed to account for the effect of eddy-topography interaction. Since the overflow areas further north are neither horizontally nor vertically well resolved, a low bias in the dense bottom water flow might also contribute to the missing north-west corner in the models. The warm bias at 50°N in the North Atlantic is most likely unrelated to biases in vertical mixing, and consequently using IDEMIX does not change much the model results here.

The mixed layer depths in the subpolar North Atlantic (supplementary Fig. C4), are increased in all models and in all experiments with IDEMIX compared to the respective reference simulations, in particular in the convectively active regions such as the Nordic Seas, Irminger, and Labrador Sea. This increase could be caused by a more efficient preconditioning for convection in case of stronger vertical mixing in the convective regions. It is largest with forcing A and smaller but similar for the other two forcing datasets. The deeper mixed layer depths are associated with an increase of the meridional overturning circulation in the Atlantic Ocean as discussed in the next section. In MITgcm-REF und ICON-REF, the mixed layer depths in the subpolar North Atlantic roughly agree with observations (Fig. C6, Locarnini et al., 2018; Zweng et al., 2019), while FESOM-REF tend to feature too deep convection depths here. In MITgcm-A und ICON-A, mixed layer depths are getting too deep in comparison with the observations, but using forcing B and C the region of deep mixing is increasing and tend to be in better agreement with the observations. In FESOM, the experiments with IDEMIX are increasing the already too deep and too large mixing region, thus increasing the model bias further.

In FESOM, mixed layer depths in the Southern Ocean also tend to be too deep compared to observations, and also increase in the experiments with IDEMIX compared to FESOM-REF, in particular in FESOM-A (supplementary Fig. C5). Related to the unrealistically deep mixed layer in FESOM-A, the warm bias in the Southern Ocean in FESOM-REF changes into a cold bias in FESOM-A (Fig. 6). Since forcing A has much larger amplitudes in the Southern Ocean and in particular in the Weddell Sea than the other two

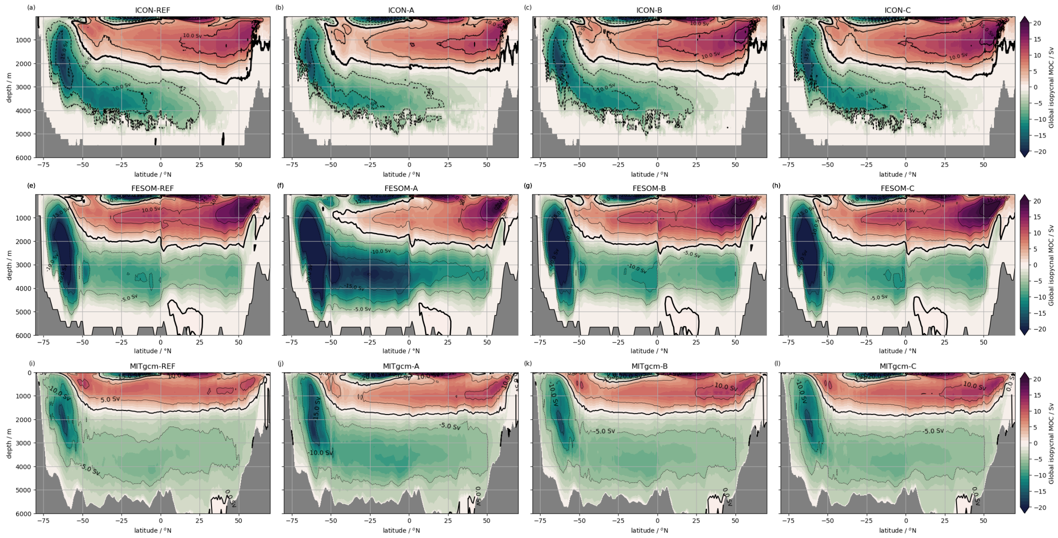

Figure 7. Global meridional overturning stream function ψ in Sv. ψ was calculated in density space and remapped to depth levels for ICON (a-d), FESOM (e-h) and MITgcm (i-l).

forcing datasets, it seems that the preconditioning by stronger mixing leads to the exaggerated deep convection in FESOM-A. This is also related to a substantially enhanced formation of bottom water in FESOM-A discussed in the next section. In ICON-A, we also see slightly increased mixed layer depth in the Weddell Sea, which may point towards too large forcing by dataset A in this region, but the other experiments with ICON and also the MITgcm show hardly any changes.

6 Effects on the circulation

The global meridional overturning stream function ψ was calculated by zonally and vertically integrating the northward transports below more than 80 isolines of the local potential density $\sigma_2(z)$ with reference pressure of 2000 dbar, and remapping to depth using $z(\bar{\sigma}_2)$, where $\bar{\sigma}_2$ denotes the zonal average of σ_2. Note that this procedure reflects better the actual watermass transports than simply averaging the transports at constant z-levels (McDougall & McIntosh, 2001). All simulations show the familiar two cell structure of the global overturning (Fig. 7). The differences in the strength and shape of the overturning cells are larger between different models than between the different experiments with each model (with the exception of FESOM-A).

While ICON and FESOM show in general stronger and deeper reaching upper cells in the northern hemisphere, MITgcm has weaker overturning there. The lower cell in the southern hemisphere is also weaker in MITgcm and stronger in ICON and FESOM. The largest difference within the experiments with each model is given by the large increase of the bottom cell in FESOM-A. In this FESOM simulation, the stronger mixing work of forcing A seems to trigger exaggerated deep water formation in the Southern Ocean that also leads to the mixed layer depth bias in Fig. C5. As a consequence, the overturning of the deep Pacific cell increases substantially. Except for the deep cell in the Southern Ocean, differences in ψ by different forcings remain relatively small, compared to the differences between the models.

Also for the decomposition of the global stream function into Atlantic and Indo-Pacific basins, the differences between the models are larger than differences between different experiments with the same model (Fig. C7 and C8 in the appendix). In all mod-

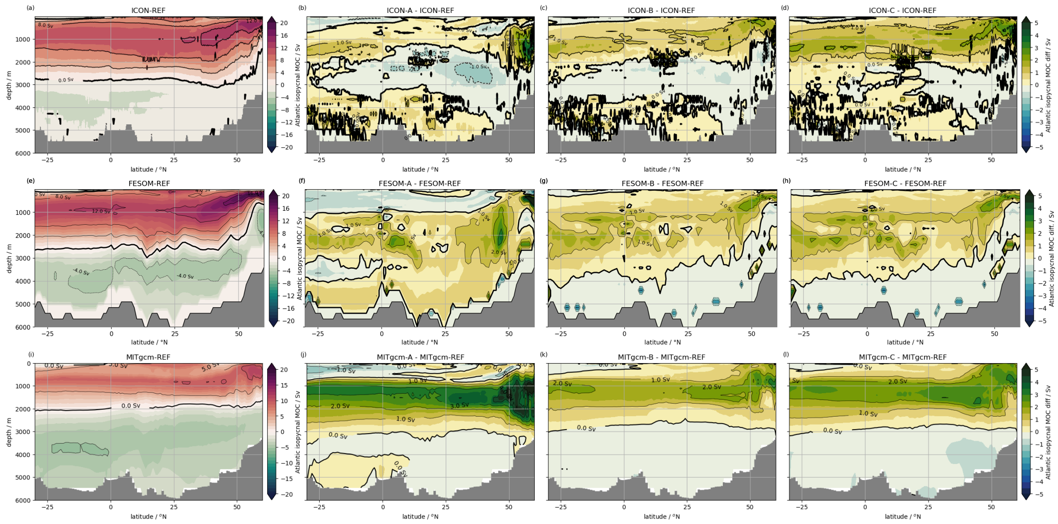

Figure 8. As Fig. 7, but for the Atlantic basin, and showing differences to the reference experiments to the sensitivity experiments with different forcings.

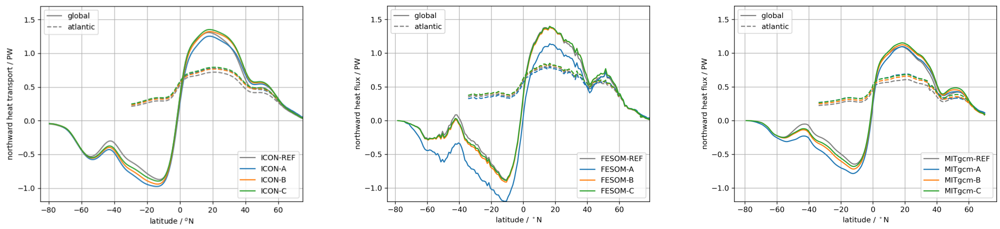

Figure 9. Northward heat transport in PW.

els, the Atlantic upper cell increases by up to 5 Sv, but the vertical shape of this increase is different between models (Fig. 8). For ICON and FESOM, the increase of the upper cell in the subtropics is largest for forcing C, but for the MITgcm is is for forcing A. The increased overturning is related to deeper mixed layers in the subpolar North Atlantic in each of the experiments with IDEMIX (compare supplementary Fig. C4), which points towards increased deep water formation. This relation between deep convection and the strength of the overturning is often seen in ocean models (e.g. Eden & Jung, 2001). However, the connection between deep water formation and overturning is still not fully understood (e.g. Lozier et al., 2019).

Compared to observations (e.g., Lumpkin & Speer, 2007) the upper cell of the Atlantic overturning is too weak in all reference simulations, in particular in the subtropics and in MITgcm-REF. Furthermore, the upper cell of the stream function is too shallow (see Korn et al., 2022; Jungclaus et al., 2022). The common model response to including IDEMIX thus tends to drive all models closer to observations. Accordingly, northward heat transports are also increased in the Atlantic Ocean (compare Fig. 9), but all models still fall short in reproducing the observed (more than 1 PW) heat transports. Changes in the lower cell in the Atlantic are weak and incoherent between the different models (Fig. 8), a feature also seen in the bottom cell of the Indo-Pacific, discussed below.

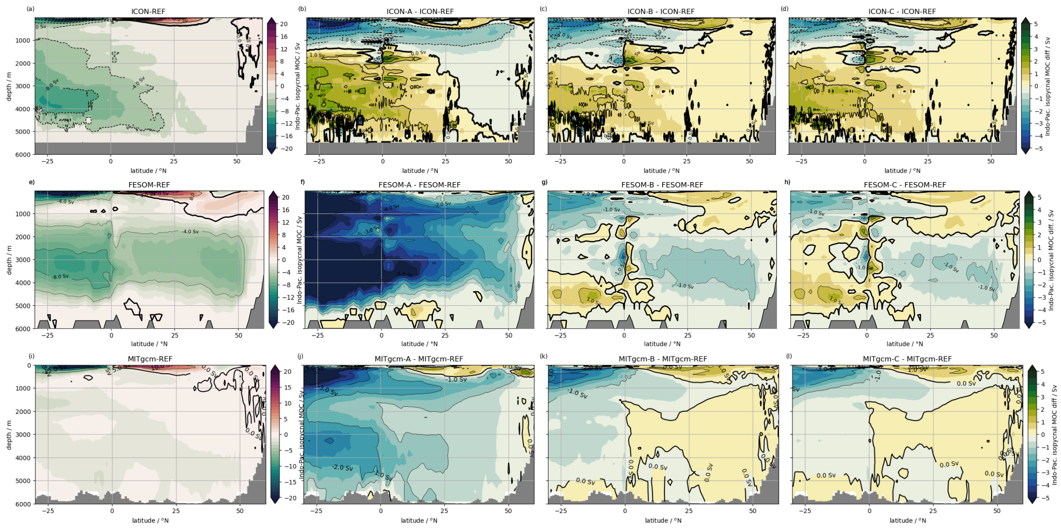

Figure 10. Same as Fig. 8, but for the Indo-Pacific basin.

In the Indo-Pacific basins, the strength of the southern upper shallow overturning cell within the thermocline increases in all models with IDEMIX compared to the reference simulations (Fig. 10). North of the equator, a similar increase of the shallow cell is also seen in ICON and MITgcm, but only to a weaker extent in FESOM. The shallow cells within the thermocline are thought to be wind-driven, therefore the common model response of an increase of the cells due to larger mixing work is surprising. However, this increase is related to a deeper thermocline in these simulations (Fig. 5), which might lead to larger areas of the subducting density layers exposed to the atmosphere and thus stronger ventilation and stronger overturning.

Substantial changes can be found in the Indo-Pacific bottom cell (Fig. 10), but no coherent response amongst the models, similar to the Atlantic bottom cell. The largest change in the Indo-Pacific can be seen in FESOM-A, which we can relate to the exaggerated deep convection in the Weddell Sea in this simulation. MITgcm-A also shows an increase in the bottom cell due to the stronger mixing in the Southern Ocean compared to the very weak cell in MITgcm-REF, but in contrast to our expectation, the bottom cell is decreasing in strength in all ICON simulations including IDEMIX and the larger mixing work. A bottom water transport estimate of 22.7±7.7 Sv into the Pacific at 32^oS from observations (Lumpkin & Speer, 2007) is not reproduced by any model, even for the unrealistic case FESOM-A (other observational estimates yield smaller transports into the Pacific). The reason for this model bias, and in particular the reason for the incoherent model response in the bottom cell in the Indo-Pacific and Atlantic Ocean remains unclear. We discuss this aspect in the next section.

7 Discussion and conclusions

A vertical mixing scheme based on internal wave physics (IDEMIX) is implemented and evaluated in three different ocean model codes: ICON-O, FESOM, and MITgcm. The implementation of IDEMIX is available at `https://github.com/nbruegge/CVMix-src`. The implemented IDEMIX version (Olbers & Eden, 2013) predicts the bulk wave energy propagation and dissipation, given the wave forcing functions at the top and the bottom. The wave energy dissipation provides forcing to an energy-based mixing closure for the effects of small-scale turbulence (Gaspar et al., 1990), and is available for mixing. The surface energy forcing for IDEMIX is small and we keep it the same in all model experiments, while we apply three different products for the bottom forcing by tidal flow over topography: forcing A is based on the drag parameterization by internal tide generation of a barotropic tidal model (Jayne & St. Laurent, 2001), forcing B is calculated from linear theory using only velocities from a barotropic tidal model and the observed topography spectrum (Nycander, 2005; Falahat et al., 2014), and forcing C is taken from a global high-resolution ocean model simulation including tidal forcing (Li & von Storch, 2020). While forcing A is subject to the biases of the barotropic tidal model for which the drag parameterization accounts for, forcing B suffers from the limitation of linear theory of shallow slopes and weak flow, and forcing C from limited horizontal resolution, dissipation and other unknown biases of the high-resolution model. Accordingly, the forcing functions differ by almost a factor of two in the global integrated flux into the wave field, where forcing A is the strongest, and B and C are similar, and represent the current uncertainty in the flux into the wave field.

The three ocean models applied here are taken as examples for typical state-of-the-art non-eddy resolving ocean-only global configurations. The surface forcing of the models is identical, while many other aspects of the models differ; the reader is referred to the references listed in the main text about details of the model configurations. It is important to note that no attempt has been made to tune the performance of the new vertical mixing scheme. The effect of the three different bottom forcing functions in the three ocean models is assessed by comparing to a reference simulation, in which the effect of breaking internal gravity waves is implemented by a threshold for minimal turbulent energy. Since the effect of new parameterizations is often model dependent, the common response in the three different models allows us to assess the model-independent effects of the IDEMIX closure. We find the following common model response:

- Common to all models is larger interior mixing work κN^2 in the global integral with larger vertical and in particular horizontal structure due to the inhomogeneous forcing functions in all simulations using IDEMIX, compared to the respective reference simulation (Fig. 2). The global underestimation in the reference simulations could be resolved by adjusting the threshold of minimal turbulent energy in the scheme of small-scale turbulent mixing, but the spatial structure will not be reproduced without IDEMIX. Note that our choice of threshold value is based on common practice in ocean modelling.
- IDEMIX improves the horizontal variations of κN^2 along 170^oW – within the large error bounds – compared to to finestructure observations. Forcing A seems to overestimate κN^2 in the South Pacific and the Southern Ocean and to underestimate it in the subtropical Pacific. The mixing work obtained with forcing B best matches the observations. All models but MITgcm tend to overestimate κN^2 in the subpolar North Pacific. However, the differences of κN^2 for the different forcing functions stay within the large error bounds of the observations.
- A rather coherent model response are the changes in the thermocline depth. In all simulations with IDEMIX the thermocline tends to become deeper compared to the respective reference simulations, although there are also regions with shallower thermocline depths (Fig. 5). This is related to cooling of the upper thermocline and warming of the lower thermocline, but local thermocline depth changes are not necessarily related to locally enhanced mixing rates. Whether these changes drive the models closer to observations (i.e., the initial conditions) turns out to be model dependent, since it may or may not compensate other model biases.
- The wind-driven shallow overturning cell in the Indo-Pacific within the thermocline increases in all models with IDEMIX (Fig. 10). Due to the deepening of the thermocline, larger areas of the subducting density layers might be exposed to the atmosphere which then leads to the stronger ventilation and stronger overturning.

- Another common model response are deeper mixed layer depths in the subpolar North Atlantic, which could be due to more efficient preconditioning of deep convection (Fig. C4). In the Southern Ocean, the energy input in forcing A leads to an unrealistic large region of deep convection in the Weddell Sea in one of the models, which is not or to a lesser extent present using the other forcing functions in the same model (Fig. C5). This artifact points towards too large and unrealistic energy input by forcing A (see above and Fig. 4b)
- The increase in mixed layer depth in the subpolar North Atlantic is related to a common increase of the upper cell of the Atlantic overturning circulation in all models, driving the models closer to observed transports in the subtropics (Figs. 8 and 10).
- The increase in the upper cell of the Atlantic overturning circulation is associated with an increase in northward heat transport in the Atlantic in all models (Fig. 9), although all models still underestimate northward heat tranports.
- The lower cell in the Atlantic and the Indo-Pacific do not show systematic changes common to all models although changes are up to a factor of two in some of the simulations (Figs. 8 and 10). The lower Indo-Pacific cell in ICON weakens when IDEMIX is included which is counter intuitive with the enhanced mixing work present in the simulation applying IDEMIX. FESOM and MITgcm show an increase of the lower Indo-Pacific cell for the stronger bottom forcing A but hardly any change for forcing B and C. Furthermore, all simulations show too low transports of the lower Indo-Pacific cell.

The reason for the circulation bias in the bottom cell of the Indo-Pacific Ocean, and the reason for the incoherent model response in the bottom cell in the Indo-Pacific and Atlantic Ocean remains unclear to us. This incoherent model response is surprising since it is commonly assumed that the bottom cells in the major ocean basins are driven by vertical mixing. On the other hand, the upper cell in the North Atlantic shows a coherent model response of an increase with stronger mixing work, although it is commonly assumed that it is driven by wind stress in the Southern Ocean and not by the vertical mixing. The increase in the upper cell in the North Atlantic is related to deeper convection in the subpolar North Atlantic, which we in turn explain by changes in preconditioning for convection by the change in vertical mixing. We cannot answer how changes in convection are related to changes in the strength of the upper cell in the North Atlantic, since there is currently no consistent dynamical framework of the dynamics of the ocean's overturning in closed basins (e.g. Straub, 1996; Greatbatch & Lu, 2003; Brüggemann et al., 2011).

Strong numerical mixing typical for coarse models may hide some of the effects the explicit vertical mixing by IDEMIX on the large-scale transports in the bottom overturning cells in the major ocean basins. Other, non-local effects may be responsible for the model biases in the bottom cells, such as deep water formation biases around the Antarctic, errors in bottom topography, or errors in the isopycnal structure of the Antarctic Circumpolar Current. Unfortunately, numerical mixing is difficult to assess. We are working on implementing methods to diagnose numerical mixing following Klingbeil et al. (2014) into the models, but for now we have to postpone a further discussion.

In any case, we could show that applying a more realistic vertical mixing parameterzations have a notable effect on the ocean circulation with partly improved model biases. The more realistic mixing parameterizations furthermore help to identify model biases since the energy available for vertical mixing is finally physically constrained. One suspicious candidate for such a model bias is numerical mixing and the results which we obtained here suggest to more carefully revisit water mass transformations and diapycnal velocities associated with this numerical mixing.

Appendix A Vertical mixing closure

In this study, we use the closure by Gaspar et al. (1990) to parameterize the mixing in the surface mixed layer, but also the mixing in the interior of the ocean in the reference experiments. The closure is based on a parameterized budget for turbulent kinetic energy E_{tke}, assuming lateral homogeneous conditions, given by

$$\partial_t E_{tke} = \partial_z c_{tke} k_m \partial_z E_{tke} + k_m \left(\partial_z \boldsymbol{u}\right)^2 + \epsilon_{iw} - kN^2 - c_\epsilon E_{tke}^{3/2} L^{-1} \tag{A1}$$

with the parameter $c_\epsilon = 0.7$ and $c_{tke} = 30.0$. ϵ_{iw} denotes the dissipation of internal wave energy and is defined below in Eq.B1. Key for the closure by Gaspar et al. (1990) is the mixing length assumption for the vertical viscosity $k_m = c_k E_{tke}^{1/2} L$ with $c_k = 0.1$, or vertical diffusivity $k = k_m/Pr$ with the Prandtl number Pr given by

$$Pr = \max\left(1, \min(10, 6.6Ri)\right) \ , \ Ri = N^2 \max\left(\left(\partial_z \boldsymbol{u}\right)^2, \epsilon_{iw}/k_m\right)^{-1} \tag{A2}$$

This formulation for Pr and Richardsen number Ri yields an equivalent interior mixing efficiency of 0.2. Note that in the reference experiments, $\epsilon_{iw} = 0$ and we set $E_{tke} = \max(E_{tke}, 10^{-6}\,\mathrm{m}^2/\mathrm{s}^2)$ at each time step, since the production of E_{tke} by the shear of the mean flow is too low in the interior. The choice of the mixing length scale L follows Blanke and Delecluse (1993) (their Eqs. 2.27 to 2.30). The closure has been implemented together with IDEMIX in the Community Vertical Mixing Project (CVMix) (Griffies et al., 2015).

Appendix B IDEMIX closure

IDEMIX (Internal Wave Dissipation, Energy and Mixing) is an internal wave model based on the radiative transfer equation, the spectral energy balance equation of internal gravity waves (Olbers & Eden, 2013). Several simplifications, most notably the integration in wavenumber space, reduce the complexity of the radiative transfer equation and lead to a partial differential equations for wave energy compartments that are simple enough to be solved online in global ocean general circulation models. Several different versions of IDEMIX have been proposed, including a low mode tidal and near-inertial wave compartment with explicitly resolved horizontal propagation (Eden & Olbers, 2014), a version including the effect of wave drag on the mean flow (Olbers & Eden, 2017; Eden & Olbers, 2017), and a version including a compartment for lee waves (Eden et al., 2021). In this study, however, we use the simplest IDEMIX approach (Olbers & Eden, 2013) as implemented in CVmix. It is given by

$$\partial_t E_{iw} = \partial_z \left(c_0 \tau_v \partial_z c_0 E_{iw}\right) + \nabla_h \cdot \tau_h v_0 \nabla_h v_0 E_{iw} - \epsilon_{iw} \ , \ \epsilon_{iw} = \mu_0 f_e \frac{m_*^2}{N^2} E_{iw}^2, \tag{B1}$$

where E_{iw} is a (single) wave energy compartment, and c_0 and v_0 bulk group velocities in vertical and horizontal direction, respectively, calculated assuming a certain spectral shape of the wave field, i.e. the Garrett-Munk (GM) model spectrum (Cairns & Williams, 1976; Munk, 1981). ϵ_{iw} represents the dissipation of wave energy by wave breaking following (Henyey et al., 1986) with $f_e = |f|\mathrm{acosh}(N/|f|)$, and is also used for the so-called fine-structure parameterization (Kunze, 2017). Note that this form for ϵ_{iw} was validated recently by Eden et al. (2019) by numerical evaluation of the scattering integral for wave-wave interactions.

The following parameters are contained in our simple IDEMIX closure:

- τ_v is a time scale on which wave-wave interactions lead to a symmetrization of the energy compartments of up- and downward propagating waves.
- τ_h is a corresponding time scale for eliminating lateral anisotropy.
- μ_0 is related to the dissipation of internal wave energy by wave-wave interactions.

- j_* is the equivalent mode number scale, related to the roll-off wavenumber m_* in the GM model spectrum by $m_* = N/c$ with $c = \int N/(j_*\pi)\mathrm{d}z$.

The parameter settings that lead to the best agreement with maps of wave energy and E_{tke} dissipation rates estimated from Argo float profiles are $\tau_v = 2\,\mathrm{d}$, $\tau_h = 15\,\mathrm{d}$, $\mu_0 = 1/3$ and $j_* = 5$ (Pollmann et al., 2017). Sensitivity tests in Pollmann et al. (2017) indicate that variations of τ_v and τ_h have very little impact on the average wave energy levels and TKE dissipation rates, whereas variations of j_* have the largest. Through its impact on the representative vertical group velocity, higher values of j_* will reduce the upper-ocean internal wave energy levels.

The generation of internal wave energy is accounted for in the vertical boundary conditions for the flux divergence term on the left-hand side of Eq. B1: at the surface, wind stress fluctuations create near-inertial oscillations of the mixed layer that can radiate internal waves of near-inertial frequency into the ocean interior, and at the bottom, the interaction of barotropic tidal currents with rough seafloor topography leads to the formation of internal tides. For the former, we update the maps used by Olbers and Eden (2013) and take instead the fraction of wind power input into near-inertial motions that leaves the mixed layer calculated by Rimac et al. (2013) and shown in Fig. 1(a). For the latter, we use three different maps, which are shown in Fig. 1(b-d).

Appendix C Tidal forcing

Tidal forcing in IDEMIX is a two-dimensional map of the barotropic-to-baroclinic energy conversion applied at the bottom. This energy conversion can be estimated in several ways: from linear theory (Bell, 1975a, 1975b), from a simple scaling based on linear theory to describe the dissipation in barotropic tide models (Arbic et al., 2018), or from three-dimensional numerical simulations forced with the lunisolar tidal potential (Niwa & Hibiya, 2011; Müller et al., 2010; Buijsman et al., 2020).

Forcing A is a simple relation for the barotropic-to-baroclinic tidal energy conversion based on linear theory:

$$E_f \sim \frac{1}{2}\rho_0 k_{topo} h^2 N |\mathbf{u}|^2, \tag{C1}$$

where h^2 is the bottom roughness, ρ_0 the density, N the buoyancy frequency, $\mathbf{u} = (u, v)$ is the horizontal velocity vector and k_{topo} the topographic wavenumber treated as a free, spatially constant parameter (Jayne & St. Laurent, 2001). It was suggested by Jayne and St. Laurent (2001) to add an associated drag term $-1/2 k_{topo} h^2 N \mathbf{u}$ as a sink to the barotropic shallow water momentum budget to account for the energy loss by internal tide generation, which led to a much better agreement with barotropic tide dissipation estimates obtained from satellite altimetry. The scaling Eq. C1 is often used in parameterizations of near-field tidal mixing in global numerical simulations (St. Laurent et al., 2002; Simmons et al., 2004; Griffies et al., 2015) and, evaluated globally for the Community Earth System Model (CESM) (Hurrell et al., 2013), also as tidal forcing in IDEMIX (Olbers & Eden, 2013). The latter is what we use as forcing A. As eq. C1 was obtained by neglecting any frequency dependence (Jayne & St. Laurent, 2001), forcing A represents all tidal constituents.

Forcing B is derived from linear theory, which builds on the work of Bell (1975a, 1975b). While Bell assumes an infinitely deep ocean, Llewellyn Smith and Young (2002) as well as Khatiwala (2003) considered a finitely deep ocean and derived the conversion into different vertical normal modes. These expressions or variants thereof have been evaluated globally a number of times: Nycander (2005), for example, performed global calculations for the 8 major constituents using Bell's theory, to which he applied a correction factor to mimic the behavior in a finitely deep ocean. Falahat et al. (2014) calculated the conversion globally for the first 10 M_2-tide modes using the approach of Llewellyn Smith and Young (2002). All linear theory approaches rely on several assumptions, i.a. that the topography be subcritical, the topographic obstacles be much smaller than the water depth, and the tidal excursion be small. To date, there is no analytically sound derivation of how to correct the relevant equations in cases when these assumptions are violated; instead, the calculations are performed everywhere and empirical corrections are added later. The advantage of the linear theory approach is that topography input of very high resolution can be used at reasonable computational costs. Here, we use the non-modal linear theory estimates of Nycander (2005) as calculated by Falahat et al. (2014) as forcing B, which represent the eight major tidal constituents M_2, S_2, N_2, K_2, K_1, O_1, P_1, Q_1.

Forcing C is derived from a three-dimensional numerical model forced with the lunisolar tidal potential. The advantage of this approach (Niwa & Hibiya, 2011; Müller et al., 2010; Buijsman et al., 2020) is that all the assumptions inherent in linear theory are irrelevant, but on the downside, not all modes are resolved and other assumptions to deal with the dissipation of the internal tide energy need to be invoked. For forcing C, we consider the M_2-tide generation in the STORMTIDE2 simulation (Li & von Storch, 2020). STORMTIDE2 was performed using the primitive-equation model MPI-OM (Max-Planck-Institute Ocean Model) (Marsland et al., 2003; Jungclaus et al., 2006) with a horizontal resolution of 0.1° and 40 vertical levels, which resolves the lowest modes of the M_2-tide. Tides are excited by applying the full luni-solar tidal potential, parameterizing self-attraction and loading effects following Thomas et al. (2001). After a 33-year long spin-up with a climatological forcing of daily resolution (Röske, 2006), the model is forced by the 6-hourly NCEP/NCAD reanalysis-1 (Kalnay et al., 1996) and integrated for the years 1981-2012. The barotropic-to-baroclinic energy conversion of the M_2-tide was evaluated for the final year of this period. Li et al. (2015) show that the relatively similar STORMTIDE simulation fully resolves the propagation of the first two M_2 tide modes. It is likely that more modes are resolved when it comes to their generation, but it is unclear how many exactly. Because the lowest modes carry most of the energy, we will in our comparison of the different tidal forcings for IDEMIX not make any correction for the unresolved higher M_2-modes and only add the seven other constituents of the computation by Nycander (2005) to obtain a total forcing agreeing with forcings A and B.

Open Research Section

The model code of ICON is available to individuals under licenses (`https://mpimet.mpg.de/en/science/modeling-with-icon/code-availability`). By downloading the ICON source code, the user accepts the licence agreement. The model code for FESOM is available under: `https://zenodo.org/record/7737061`. The model code for MITgcm can be found under `https://github.com/MITgcm/MITgcm`, specific modifications, configuration, and plotting scripts can be found under `https://github.com/mjlosch/MITgcm/tree/idemix_test_runs`.

The source code of the specific ICON-O version used in this study, the configuration files for the ICON simulations, and the post-processing scripts for ICON, FESOM and the observational data can be found under `https://hdl.handle.net/21.11116/0000-000C-DE5C-4`. The ICON plots were made by making use of the ICON post-processing toolbox pyicon (`https://gitlab.dkrz.de/m300602/pyicon`) and the FESOM plots were made by making use of tripyview (`https://github.com/FESOM/tripyview`).

The CVMix implementation of IDEMIX and the TKE scheme which are used by ICON and FESOM can be found within the corresponding model source codes and under `https://github.com/nbruegge/CVMix-src`. MITgcm used an equivalent implementation of IDEMIX and the TEK scheme which can be found within the MITgcm source code (see link above).

The tidal forcing of Nycander (2005) and Falahat et al. (2014) was obtained from `https://www.seanoe.org/data/00470/58153/`, using the corrected form of the modal calculations of Falahat et al. (2014) provided by de Lavergne et al. (2019). The tidal forcing based on the scaling by Jayne (2009) is the same as used in CESM simulations, which we obtained from their subversion server `https://svn-ccsm-inputdata.cgd.ucar.edu/trunk/inputdata/ocn/pop/gx1v6/forcing/`.

The observational references were obtained from `https://ftp.nwra.com/outgoing/kunze/iwturb/` (Kunze, 2017). The global topography dataset of Becker et al. (2009) can be downloaded from `https://topex.ucsd.edu/marine_topo/`.

Acknowledgments

This paper is a contribution to the Collaborative Research Centre TRR 181 "Energy Transfers in Atmosphere and Ocean" funded by the Deutsche Forschungsgemeinschaft (DFG, German Research Foundation) - Projektnummer 274762653. This work used resources of the Deutsches Klimarechenzentrum (DKRZ) granted by its Scientific Steering Committee (WLA) under project ID bm1239.

References

Adcroft, A., & Campin, J.-M. (2004). Rescaled height coordinates for accurate representation of free-surface flows in ocean circulation models. *Ocean Modelling*, *7*(3), 269–284. Retrieved from `http://www.sciencedirect.com/science/article/pii/S1463500303000544` doi: 10.1016/j.ocemod.2003.09.003

Arbic, B. K., Alford, M. H., Ansong, J. K., Buijsman, M. C., Ciotti, R. B., Farrar, J. T., ... others (2018). A primer on global internal tide and internal gravity wave continuum modeling in HYCOM and MITgcm. *New frontiers in operational oceanography*.

Becker, J., Sandwell, D., Smith, W., Braud, J., Binder, B., Depner, J., ... others (2009). Global bathymetry and elevation data at 30 arc seconds resolution: Srtm30_plus. *Marine Geodesy*, *32*(4), 355–371.

Bell, T. (1975a). Lee waves in stratified flows with simple harmonic time dependence. *J. Fluid Mech.*, *67*(4), 705–722.

Bell, T. (1975b). Topographically generated internal waves in the open ocean. *J. Geophys. Res.*, *80*(3), 320–327.

Blanke, B., & Delecluse, P. (1993). Variability of the tropical atlantic ocean simulated by a general circulation model with two different mixed-layer physics. *Journal of Physical Oceanography*, *23*(7), 1363–1388.

Brüggemann, N., Eden, C., & Olbers, D. (2011). A dynamically consistent closure for zonally averaged ocean models. *J. Phys. Oceanogr.*, *41*(11), 2242–2258.

Buijsman, M. C., Stephenson, G. R., Ansong, J. K., Arbic, B. K., Green, J. M., Richman, J. G., ... Zhao, Z. (2020). On the interplay between horizontal resolution and wave drag and their effect on tidal baroclinic mode waves in realistic global ocean simulations. *Ocean Modelling*, *152*, 101656.

Cairns, J. L., & Williams, G. O. (1976). Internal wave observations from a midwater float. *J. Geophys. Res.*, *81*(12), 1943–1950.

Danilov, S., Sidorenko, D., Wang, Q., & Jung, T. (2017). The finite-volume sea ice–ocean model (FESOM2). *Geoscientific Model Development*, *10*(2), 765–789.

de Lavergne, C., Falahat, S., Madec, G., Roquet, F., Nycander, J., & Vic, C. (2019). Toward global maps of internal tide energy sinks. *Ocean Modelling*, *137*, 52–75.

Eden, C., & Jung, T. (2001). North atlantic interdecadal variability: oceanic response to the north atlantic oscillation (1865–1997). *Journal of Climate*, *14*(5), 676–691.

Eden, C., & Olbers, D. (2014). An energy compartment model for propagation, nonlinear interaction, and dissipation of internal gravity waves. *Journal of Physical Oceanography*, *44*(8), 2093–2106.

Eden, C., & Olbers, D. (2017). A closure for internal wave–mean flow interaction. Part II: Wave drag. *Journal of Physical Oceanography*, *47*(6), 1403–1412.

Eden, C., Olbers, D., & Eriksen, T. (2021). A closure for lee wave drag on the large-scale ocean circulation. *Journal of Physical Oceanography*, *51*(12), 3573–3588.

Eden, C., Pollmann, F., & Olbers, D. (2019). Numerical evaluation of energy transfers in internal gravity wave spectra of the ocean. *Journal of Physical Oceanography*, *49*(3), 737–749.

Falahat, S., Nycander, J., Roquet, F., & Zarroug, M. (2014). Global calculation of tidal energy conversion into vertical normal modes. *J. Phys. Oceanogr.*, *44*(12), 3225–3244. doi: https://doi.org/10.1175/JPO-D-14-0002.1

Ferreira, D., Marshall, J., & Heimbach, P. (2005). Estimating eddy stresses by fitting dynamics to observations using a residual-mean ocean circulation model and its adjoint. *J. Phys. Oceanogr.*, *35*, 1891-1910.

Forget, G., Campin, J.-M., Heimbach, P., Hill, C. N., Ponte, R. M., & Wunsch, C. (2015). ECCO version 4: an integrated framework for non-linear inverse modeling and global ocean state estimation. *Geoscientific Model Development*, *8*(10), 3071–3104. Retrieved from `https://gmd.copernicus.org/articles/8/3071/2015/` doi: 10.5194/gmd-8-3071-2015

Gaspar, P., Grégoris, Y., & Lefevre, J.-M. (1990). A simple eddy kinetic energy model for simulations of the oceanic vertical mixing: Tests at station Papa and long-term upper ocean study site. *J. Geophys. Res. Oceans*, *95*(C9), 16179–16193. doi: 10.1029/JC095iC09p16179

Gent, P. R., Willebrand, J., McDougall, T. J., & McWilliams, J. C. (1995). Parameterizing eddy-induced tracer transports in ocean circulation models. *Journal of Physical Oceanography*, *25*(4), 463–474.

Greatbatch, R., & Lu, J. (2003). Reconciling the Stommel Box Model with the Stommel–Arons Model: A Possible Role for Southern Hemisphere Wind Forcing? *J. Phys. Oceanogr.*, *33*, 1618–1632.

Gregg, M. C. (1989). Scaling turbulent dissipation in the thermocline. *Journal of Geophysical Research: Oceans*, *94*(C7), 9686–9698.

Griffies, S. M., Levy, M., Adcroft, A. J., Danabasoglu, G., Hallberg, R. W., Jacobsen, D., ... Ringler, T. (2015). *Theory and numerics of the community ocean vertical mixing (cvmix) project* ( ). : NOA/GFDL, NCAR, LANL.

Harris, P. T., Macmillan-Lawler, M., Rupp, J., & Baker, E. K. (2014). Geomorphology of the oceans. *Marine Geology*, *352*, 4–24.

Henyey, F., Wright, J., & Flatté, S. (1986). Energy and action flow through the internal wave field: An eikonal approach. *J. Geophys. Res.*, *91*(C7), 8487–8495.

Hurrell, J. W., Holland, M. M., Gent, P. R., Ghan, S., Kay, J. E., Kushner, P. J., ... others (2013). The community earth system model: a framework for collaborative research. *Bull. Amer. Meteor. Soc.*, *94*(9), 1339–1360.

Jayne, S. R. (2009). The impact of abyssal mixing parameterizations in an ocean general circulation model. *J. Phys. Oceanogr.*, *39*(7), 1756–1775. doi: https://doi.org/10.1175/2009JPO4085.1

Jayne, S. R., & St. Laurent, L. C. (2001). Parameterizing tidal dissipation over rough topography. *Geophys. Res. Lett.*, *28*(5), 811–814. doi: https://doi.org/10.1029/2000GL012044

Jungclaus, J. H., Keenlyside, N., Botzet, M., Haak, H., Luo, J.-J., Latif, M., ... Roeckner, E. (2006). Ocean circulation and tropical variability in the coupled model ECHAM5/MPI-OM. *Journal of climate*, *19*(16), 3952–3972.

Jungclaus, J. H., Lorenz, S. J., Schmidt, H., Brovkin, V., Brüggemann, N., Chegini, F., ... others (2022). The ICON earth system model version 1.0. *Journal of Advances in Modeling Earth Systems*, *14*(4), e2021MS002813.

Kalnay, E., Kanamitsu, M., Kistler, R., Collins, W., Deaven, D., Gandin, L., ... others (1996). The NCEP/NCAR 40-year reanalysis project. *Bull. Amer. Meteor. Soc.*, *77*(3), 437–472.

Kelly, S., & Nash, J. (2010). Internal-tide generation and destruction by shoaling internal tides. *Geophysical Research Letters*, *37*(23).

Khatiwala, S. (2003). Generation of internal tides in an ocean of finite depth: analytical and numerical calculations. *Deep-Sea Res.*, *50*(1), 3–21.

Klingbeil, K., Mohammadi-Aragh, M., Gräwe, U., & Burchard, H. (2014). Quantification of spurious dissipation and mixing–discrete variance decay in a finite-volume framework. *Ocean Modelling*, *81*, 49–64.

Korn, P. (2018). A structure-preserving discretization of ocean parametrizations on unstructured grids. *Ocean Modelling*, *132*, 73–90.

Korn, P., Brüggemann, N., Jungclaus, J. H., Lorenz, S., Gutjahr, O., Haak, H., ... others (2022). Icon-o: The ocean component of the icon earth system model—global simulation characteristics and local telescoping capability. *Journal of Advances in Modeling Earth Systems*, *14*(10), e2021MS002952.

Kunze, E. (2017). Internal-wave-driven mixing: Global geography and budgets. *J. Phys. Oceanogr.*, *47*(6), 1325–1345.

Kunze, E., Firing, E., Hummon, J. M., Chereskin, T. K., & Thurnherr, A. M. (2006). Global abyssal mixing inferred from lowered adcp shear and ctd strain profiles. *Journal of Physical Oceanography*, *36*(8), 1553–1576.

Large, W. G., McWilliams, J. C., & Doney, S. C. (1994). Oceanic vertical mixing: A review and a model with a nonlocal boundary layer parameterization. *Rev. Geophys.*, *32*(4), 363–403.

Large, W. G., & Yeager, S. G. (2009). The global climatology of an interannually varying air–sea flux data set. *Clim. Dyn.*, *33*, 341–364. doi: https://doi.org/10.1007/s00382-008-0441-3

Li, Z., Storch, J.-S. v., & Müller, M. (2015). The M2 internal tide simulated by a 1/10° OGCM. *J. Phys. Oceanogr.*, *45*(12), 3119–3135.

Li, Z., & von Storch, J.-S. (2020). M2 Internal-Tide Generation in STORMTIDE2. *J. Geophys. Res. Oceans*, *125*(8), e2019JC015453. doi: https://doi.org/10.1029/2019JC015453

Llewellyn Smith, S. G., & Young, W. (2002). Conversion of the barotropic tide. *J. Phys. Oceanogr.*, *32*(5), 1554–1566.

Locarnini, M., Mishonov, A., Baranova, O., Boyer, T., Zweng, M., Garcia, H., ... others (2018). *World Ocean Atlas 2018, Volume 1: Temperature.*

Lozier, M. S., Li, F., Bacon, S., Bahr, F., Bower, A. S., Cunningham, S. A., ... Zhao, J. (2019, February). A sea change in our view of overturning in the subpolar North Atlantic. *Science*, *363*(6426), 516–521. Retrieved from `http://science.sciencemag.org/content/363/6426/516.abstract`

Lumpkin, R., & Speer, K. (2007). Global ocean meridional overturning. *J. Phys. Oceanogr.*, *37*(10), 2550–2562.

Marshall, J., Adcroft, A., Hill, C., Perelman, L., & Heisey, C. (1997). A Finite-Volume, Incompressible Navier Stokes Model for Studies of the Ocean on Parallel Computers. *J. Geophys. Res.*, *102*(C3), 5753–5766. doi: 10.1029/96JC02775

Marsland, S. J., Haak, H., Jungclaus, J. H., Latif, M., & Röske, F. (2003). The Max-Planck-Institute global ocean/sea ice model with orthogonal curvilinear coordinates. *Ocean Modelling*, *5*(2), 91–127.

McDougall, T. J., & McIntosh, P. C. (2001). The temporal-residual-mean velocity. Part II: Isopycnal interpretation and the tracer and momentum equations. *Journal of Physical Oceanography*, *31*(5), 1222–1246.

Mortimer, N., Campbell, H. J., Tulloch, A. J., King, P. R., Stagpoole, V. M., Wood, R. A., ... others (2017). Zealandia: Earth's hidden continent. *GSA today*, *27*(3), 27–35.

Müller, M., Haak, H., Jungclaus, J., Sündermann, J., & Thomas, M. (2010). The effect of ocean tides on a climate model simulation. *Ocean Modelling*, *35*(4), 304–313.

Müller, P., Holloway, G., Henyey, F., & Pomphrey, N. (1986, August). Nonlinear interactions among internal gravity waves. *Rev. Geophys.*, *24*(3), 493–536. Retrieved from `https://doi.org/10.1029/RG024i003p00493` doi: 10.1029/RG024i003p00493

Munk, W. (1981). Internal waves and small-scale processes. In B. A. Warren & C. Wunsch (Eds.), *Evolution of physical oceanography* (pp. 264–291). MIT Press, Cambridge, MA.

Munk, W., & Wunsch, C. (1998). Abyssal recipes II: energetics of tidal and wind mixing. *Deep Sea Research Part I: Oceanographic Research Papers*, *45*(12), 1977–2010. Retrieved from `http://www.sciencedirect.com/science/article/pii/S0967063798000703`

Niwa, Y., & Hibiya, T. (2011). Estimation of baroclinic tide energy available for deep ocean mixing based on three-dimensional global numerical simulations. *J. Oceanogr.*, *67*(4), 493–502.

Nycander, J. (2005). Generation of internal waves in the deep ocean by tides. *J. Geophys. Res. Oceans*, *110*(C10). doi: https://doi.org/10.1029/2004JC002487

Olbers, D. (1983, August). Models of the oceanic internal wave field. *Rev. Geophys.*, *21*(7), 1567–1606. Retrieved from `https://doi.org/10.1029/RG021i007p01567` doi: 10.1029/RG021i007p01567

Olbers, D., & Eden, C. (2013). A global model for the diapycnal diffusivity induced by internal gravity waves. *J. Phys. Oceanogr.*, *43*(8), 1759–1779. doi: https://doi.org/10.1175/JPO-D-12-0207.1

Olbers, D., & Eden, C. (2017). A closure for internal wave–mean flow interaction. Part I: Energy conversion. *Journal of Physical Oceanography*, *47*(6), 1389–1401.

Olbers, D., Jurgenowski, P., & Eden, C. (2020). A wind-driven model of the ocean surface layer with wave radiation physics. *Ocean Dynamics*, *70*(8), 1067–1088. Retrieved from `https://doi.org/10.1007/s10236-020-01376-2` doi: 10.1007/s10236-020-01376-2

Pacanowski, R., & Philander, S. (1981). Parameterization of vertical mixing in numerical models of tropical oceans. *J. Phys. Oceanogr.*, *11*(11), 1443–1451.

Pollmann, F., Eden, C., & Olbers, D. (2017). Evaluating the global internal wave model idemix using finestructure methods. *J. Phys. Oceanogr.*, *47*(9), 2267–2289.

Polzin, K. L., & Lvov, Y. V. (2011). Toward Regional Characterizations of the Oceanic Internal Wavefield. *Rev. Geophys.*, *49*(4), RG4003–. Retrieved from `http://dx.doi.org/10.1029/2010RG000329`

Polzin, K. L., Naveira Garabato, A. C., Huussen, T. N., Sloyan, B. M., & Waterman, S. (2014). Finescale parameterizations of turbulent dissipation. *J. Geophys. Res. Oceans*, *119*(2), 1383–1419.

Redi, M. H. (1982). Oceanic isopycnal mixing by coordinate rotation. *J. Phys. Oceanogr.*, *12*(10), 1154–1158. doi: 10.1175/1520-0485(1982)012⟨1154:OIMBCR⟩2.0.CO;2

Rimac, A., von Storch, J.-S., Eden, C., & Haak, H. (2013). The influence of high-resolution wind stress field on the power input to near-inertial motions in the ocean. *Geophys. Res. Lett.*, *40*(18), 4882–4886. Retrieved from `https://doi.org/10.1002/grl.50929` doi: 10.1002/grl.50929

Röske, F. (2006). A global heat and freshwater forcing dataset for ocean models. *Ocean Modelling*, *11*(3-4), 235–297.

Scholz, P., Sidorenko, D., Danilov, S., Wang, Q., Koldunov, N., Sein, D., & Jung, T. (2022). Assessment of the Finite-VolumE Sea ice–Ocean Model (FESOM2.0) – Part 2: Partial bottom cells, embedded sea ice and vertical mixing library

CVMix. *Geosci. Model Dev.*, *15*, 335–363. doi: https://doi.org/10.5194/gmd-15-335-2022
Simmons, H. L., Jayne, S. R., Laurent, L. C. S., & Weaver, A. J. (2004). Tidally driven mixing in a numerical model of the ocean general circulation. *Ocean Modelling*, *6*(3-4), 245–263.
Steele, M., Morley, R., & Ermold, W. (2001). PHC: A global ocean hydrography with a high-quality Arctic Ocean. *J. Climate*, *14*, 2,079–2,087. Retrieved from {http://psc.apl.washington.edu/Climatology.html}
St. Laurent, L., Simmons, H., & Jayne, S. (2002). Estimating tidally driven mixing in the deep ocean. *Geophys. Res. Lett.*, *29*(23), 21–1.
Straub, D. (1996). An inconsistency between two classical models of the ocean buoyancy driven circulation. *Tellus A*, *48*(3), 477–481.
Thomas, M., Sündermann, J., & Maier-Reimer, E. (2001). Consideration of ocean tides in an OGCM and impacts on subseasonal to decadal polar motion excitation. *Geophys. Res. Lett.*, *28*(12), 2457–2460.
Tsujino, H., Urakawa, S., Nakano, H., Small, R. J., Kim, W. M., Yeager, S. G., … Yamazaki, D. (2018). JRA-55 based surface dataset for driving ocean–sea-ice models (JRA55-do). *Ocean Modelling*, *130*, 79-139. doi: https://doi.org/10.1016/j.ocemod.2018.07.002
Vic, C., Garabato, A. C. N., Green, J. M., Waterhouse, A. F., Zhao, Z., Melet, A., … Stephenson, G. R. (2019). Deep-ocean mixing driven by small-scale internal tides. *Nature Communications*, *10*(1), 1–9.
Visbeck, M., Marshall, J., Haine, T., & Spall, M. (1997). Specification of Eddy Transfer Coefficients in Coarse-Resolution Ocean Circulation Models. *J. Phys. Oceanogr.*, *27*(3), 381–402. Retrieved from http://dx.doi.org/10.1175/1520-0485(1997)027<0381:SOETCI>2.0.CO;2 doi: 10.1175/1520-0485(1997)027⟨0381:SOETCI⟩2.0.CO;2
von Storch, J.-S., & Lüschow, V. (2023, February). Wind power input to ocean near-inertial waves diagnosed from a 5-km global coupled atmosphere-ocean general circulation model. *J. Geophys. Res. Oceans*, *128*(2), e2022JC019111. Retrieved from https://doi.org/10.1029/2022JC019111 doi: 10.1029/2022JC019111
Zweng, M., Seidov, D., Boyer, T., Locarnini, M., Garcia, H., Mishonov, A., … others (2019). *World Ocean Atlas 2018, Volume 2: Salinity.*

Supplementary figures

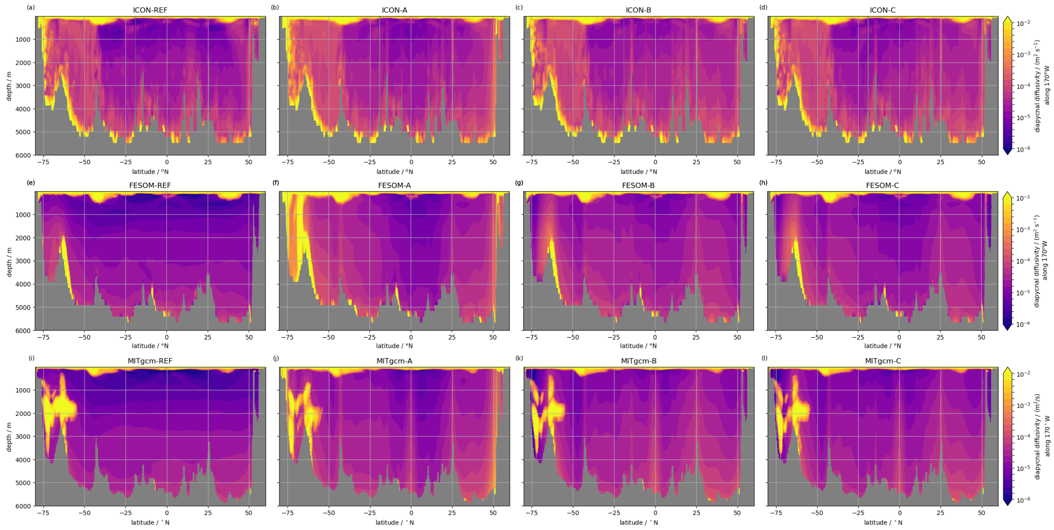

Figure C1. Diapycnal diffusivity κ along 170°W for ICON (a-d), FESOM (e-h) and MITgcm (i-l).

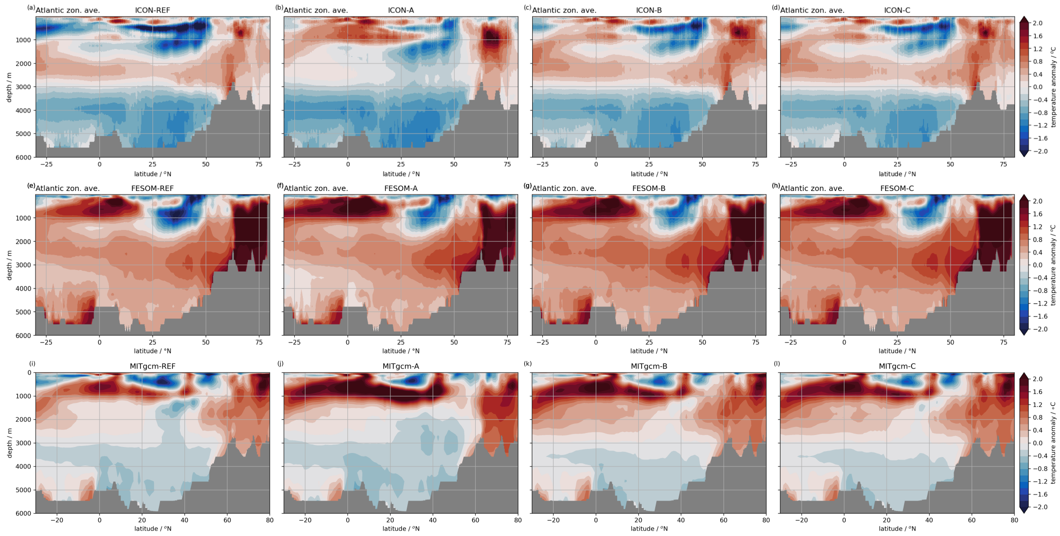

Figure C2. Atlantic zonal average of the temperature bias with respect to initial conditions for ICON (a-d), FESOM (e-h) and MITgcm (i-l).

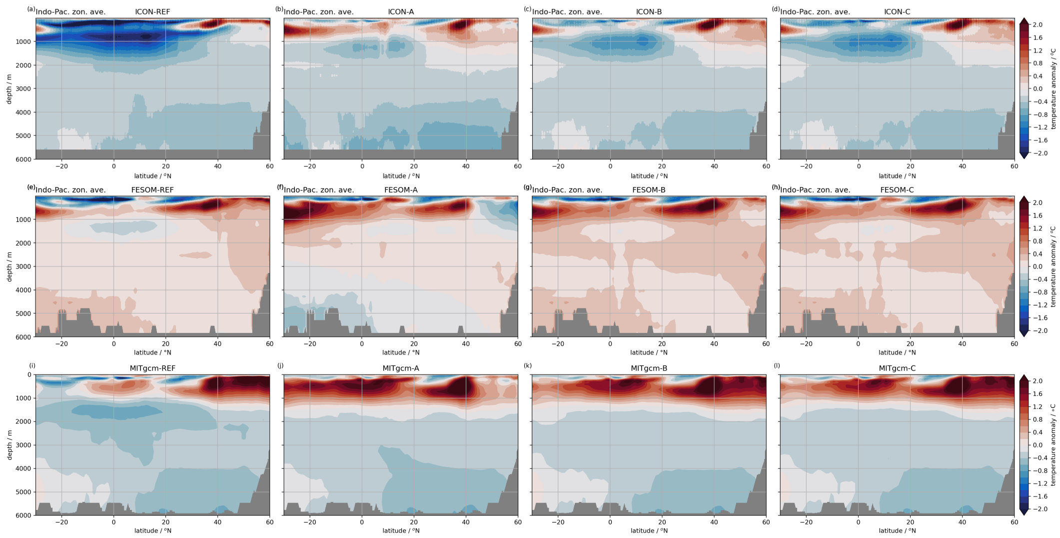

Figure C3. Indo-Pacific zonal average of the temperature bias with respect to initial conditions for ICON (a-d), FESOM (e-h) and MITgcm (i-l).

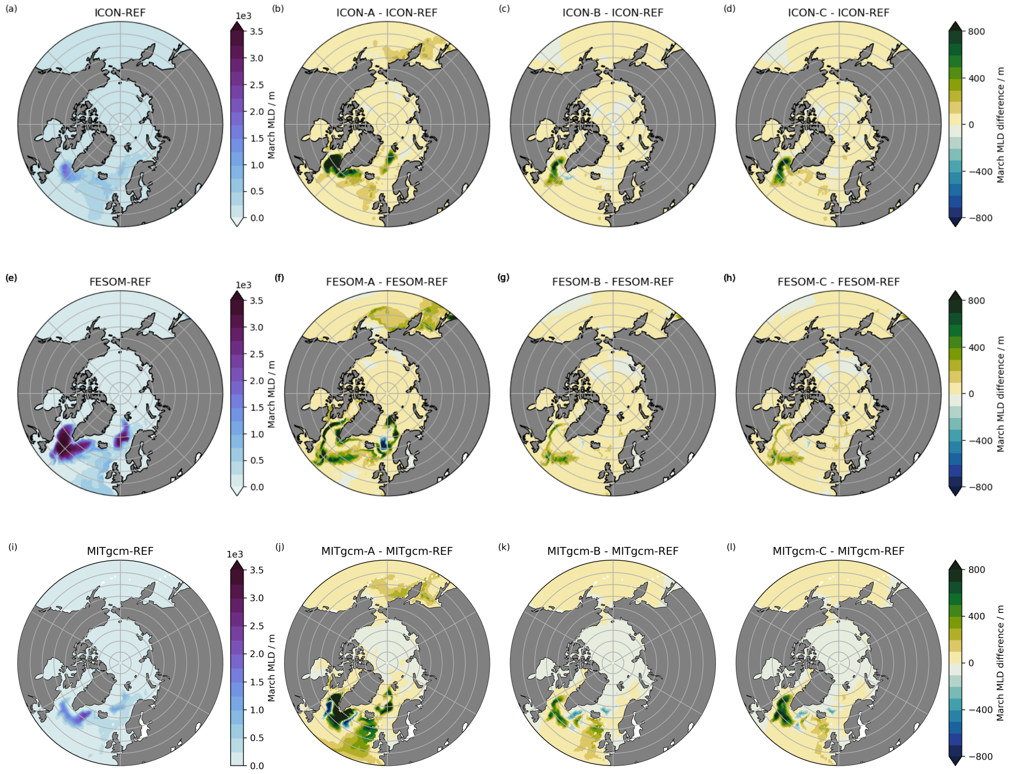

Figure C4. Mean mixed layer depth in March.

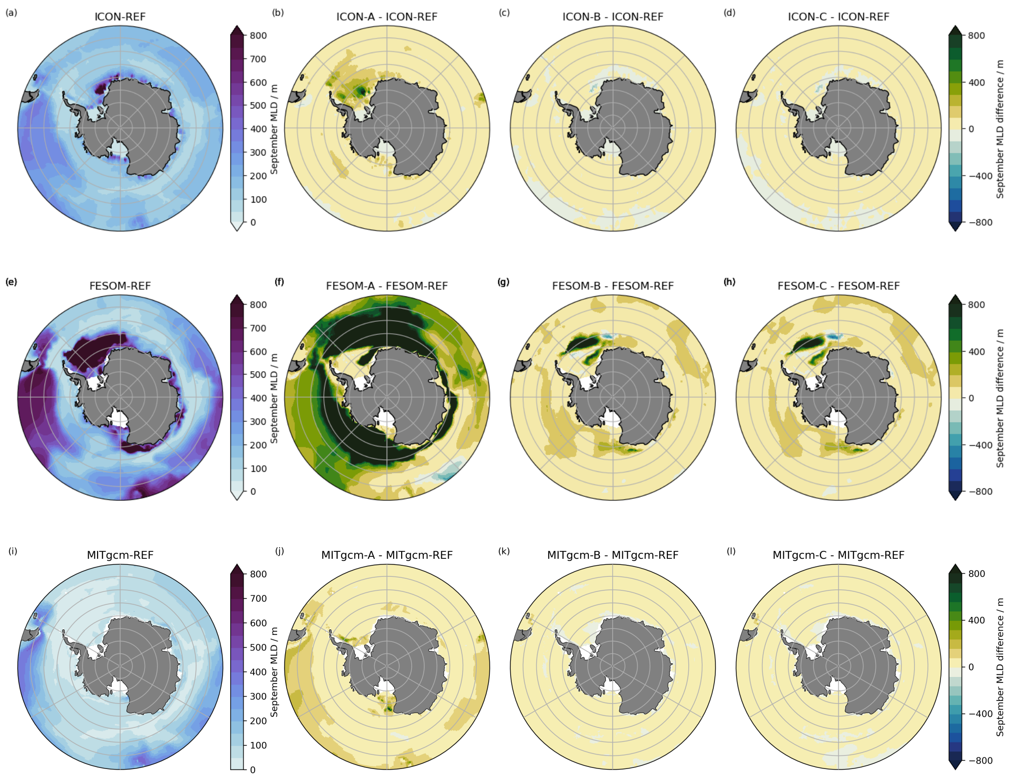

Figure C5. Mean mixed layer depth in September.

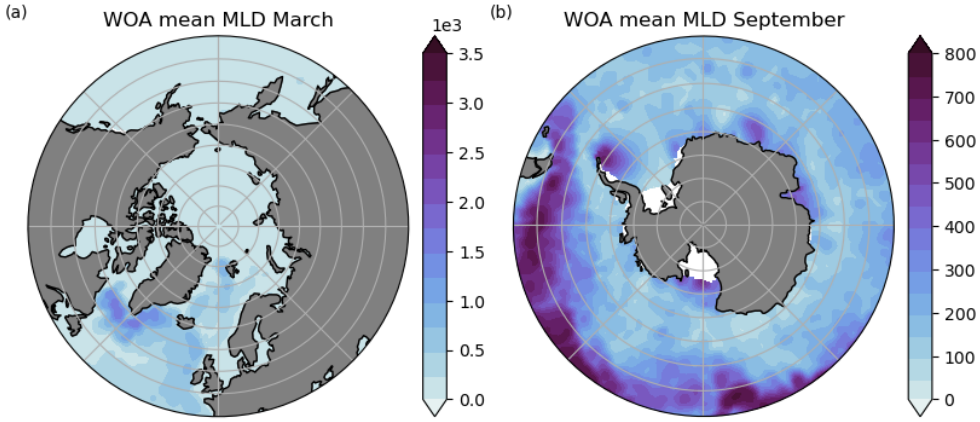

Figure C6. Mixed layer depth from the World Ocean Atlas 2018 (Locarnini et al., 2018; Zweng et al., 2019) for March (a) and September (b).

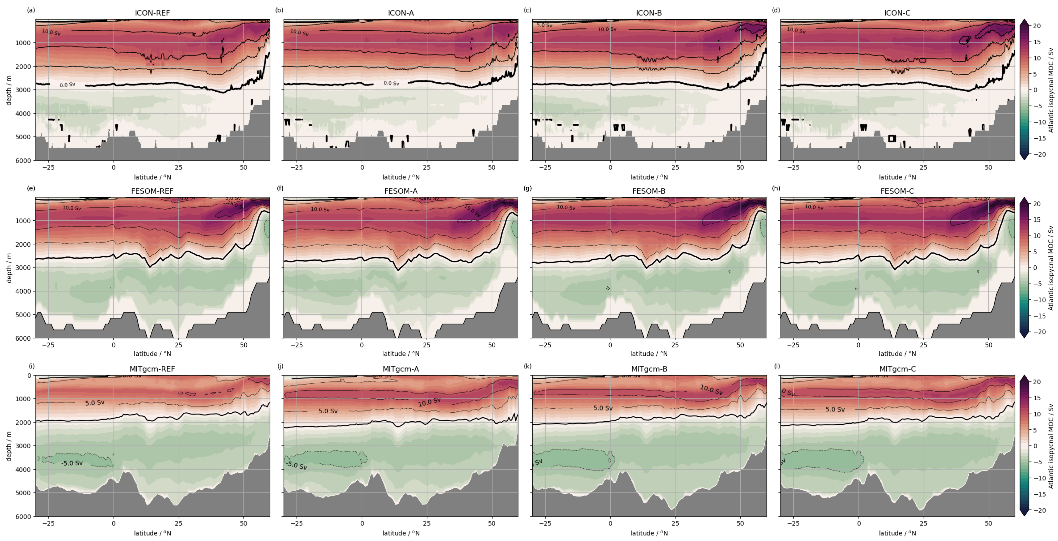

Figure C7. Atlantic meridional overturning in density space remapped to depth levels for ICON (a-d), FESOM (e-h) and MITgcm (i-l).

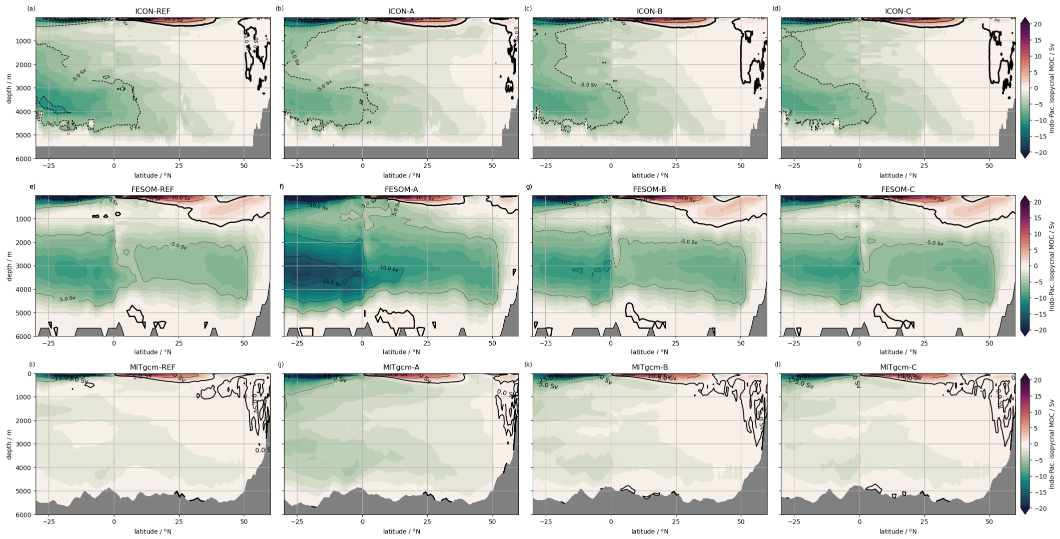

Figure C8. Indo-Pacific meridional overturning in density space remapped to depth levels for ICON (a-d), FESOM (e-h) and MITgcm (i-l).